15 MICRON *INFRARED SPACE OBSERVATORY*[1] OBSERVATIONS OF THE 1415+52 CANADA-FRANCE REDSHIFT SURVEY FIELD: THE COSMIC STAR FORMATION RATE AS DERIVED FROM DEEP ULTRAVIOLET, OPTICAL, MID-INFRARED, AND RADIO PHOTOMETRY

H. FLORES,[2] F. HAMMER,[2] T. X. THUAN,[3] C. CÉSARSKY,[4] F. X. DESERT,[5] A. OMONT,[6] S. J. LILLY,[7] S. EALES,[8] D. CRAMPTON,[9] AND O. LE FÈVRE[2]

ABSTRACT

The Canada-France Redshift Survey 1452+52 field has been deeply imaged with the *Infrared Space Observatory* using ISOCAM through the LW3 filter (12–18 μm). Careful data analysis and comparison with deep optical and radio data have allowed us to generate a catalog of 78 15 μm sources with both radio and optical identifications. They are redder and lie at higher redshift than *I*-band–selected galaxies, with most of them being star-forming galaxies. We have considered the galaxies detected at radio and 15 μm wavelengths, which potentially include all strong and heavily extincted starbursts, up to $z = 1$. Spectral energy distributions (SEDs) for each of the sources have been derived using deep radio, mid-IR, near-IR, optical, and UV photometry. The sources were then spectrally classified by comparing with SEDs of well-known nearby galaxies. By deriving their far-IR luminosities by interpolation, we can estimate their star formation rate (SFR) in a way that does not depend sensitively on the extinction. Between 35% and 85% of the star formation at $z \leq 1$ is related to IR emission, and the global extinction is in the range $A_V = 0.5$–0.85. While heavily extincted starbursts with SFRs in excess of 100 $M_\odot$ yr^{-1} constitute less than 1% of all galaxies, they contribute about 18% of the SFR density out to $z = 1$. Their morphologies range from S0 to Sab, and more than a third are interacting systems. The SFR derived by far-IR fluxes is likely to be ~ 2.9 times higher than those previously estimated from UV fluxes. The derived stellar mass formed since the redshift of 1 could be too high when compared with the present-day stellar mass density. This might be due to an initial mass function in distant star-forming galaxies different from the solar neighborhood one or an underestimate of the local stellar mass density.

Subject headings: galaxies: photometry — galaxies: starburst — galaxies: stellar content — infrared: galaxies

1. INTRODUCTION

The 2800 Å and [O II] 3727 emission-line luminosity densities have decreased by a factor of ~ 10 from $z = 1$ to the present day (Lilly et al. 1996; Hammer et al. 1997). This has led Madau et al. (1996) and Madau, Pozzetti, & Dickinson (1998) to suggest that the cosmic star formation density has decreased by the same factor within that redshift interval and that most of the stars seen now were formed during the first half of the universe's existence. The UV emission from galaxies is produced by a complex mix of short- and moderately long-lived stars, the latter (late B and A0 stars) contributing more at longer UV wavelengths. Even old stars in luminous early-type and quiescent galaxies can contribute to the observed UV luminosity density. However, the most important uncertainty in estimating the star formation density from the UV luminosity density is

due to the extinction, which can show large variations from one galaxy to another. For example, in IRAS star-forming galaxies, most of the energy is re-emitted at far-IR (FIR) wavelengths, and these objects are either missed or their star formation rates are severely underestimated when derived by UV measurements. This is why it is often thought that the UV luminosity density is likely to provide only a lower limit to the actual star formation density. The situation is complicated further by the expected contamination by active galactic nuclei (AGNs) to the UV light density. In an attempt to better estimate the cosmic star formation density, Tresse & Maddox (1998) have calculated the extinction-corrected Hα luminosity density at $z \sim 0.2$. Their result is in agreement with the UV (2800 Å) at $z = 0.35$ (Lilly et al. 1996) if an extinction of 1 mag is assumed for the UV continuum. A preliminary study of more distant galaxies indicates that the situation might be similar at $z \sim 1$ (Glazebrook et al. 1998), but it is limited by the difficulty of measuring the near-IR redshifted Hα line of faint galaxies with 4 m telescopes. Multiwavelength analyses can provide, in principle, a detailed budget of the energy output in each wavelength range for the entire galaxy energy distribution. It has been shown for local galaxies that FIR luminosities are tightly correlated with radio luminosities (Helou et al. 1988; Condon 1992) and bolometric luminosities are most closely proportional to 12 μm luminosities (Spinoglio & Malkan 1989; Spinoglio et al. 1995). These trends hold over a wide range of galaxy luminosities, despite the large variety of galaxy energy distributions. Only AGNs, which are believed to be associated to supermassive black holes, appear not to follow those rela-

[2] Observatoire de Paris, Section de Meudon, DAEC, 92195 Meudon Principal Cedex, France.

[3] Astronomy Department, University of Virginia.

[4] Service d'Astrophysique, CEA, France.

[5] Institut d'Astrophysique Spatiale, Orsay. France.

[6] Institut d'Astrophysique de Paris, France.

[7] Department of Astronomy, University of Toronto, Toronto, Canada.

[8] University of Cardiff, UK.

[9] Dominion Astrophysical Observatory, National Research Council of Canada, Victoria, Canada; flores@obspm.fr.

tions (Condon & Roderick 1988). Recent observational advances now allow us to study distant galaxies from the UV to the radio, sampling a wavelength range that covers most of the domain where their energy is being emitted. VLA deep surveys are able to detect sources down to 10 μJy (e.g., the 5 GHz surveys of Fomalont et al. 1991; Richards et al. 1998), and ISOCAM (Césarsky et al. 1996) on board the *Infrared Space Observatory* (*ISO*; Kessler et al. 1996) can reach detection limits of 100 μJy at 15 μm (Elbaz et al. 1998). In the range 60–200 μm, the detection limits are 0.2 Jy at 60μm from the IRAS faint source catalog (Moshir 1989) and 0.1 Jy at 175 μm from the FIRBACK survey carried out with *ISO* (Clements et al. 1998; Puget et al. 1998). FIR detections thus appear to be not sensitive enough to reach the same depth as radio and mid-IR (MIR) deep surveys. For example, if we consider a strong and highly reddened starburst (SBH in the terminology of Schmitt et al. 1997), a $S_{15\mu m} = 250$ μJy source would correspond to a 0.009 Jy source at 60 μm, and a $z = 1$ redshifted SBH with $S_{5GHz} = 16$ μJy would have 0.022 Jy at 175 μm. The sensibility and high spatial resolution of ISOCAM allow the study of distant field galaxies at MIR wavelengths ($2 \leq \lambda \leq 20$ μm). Star-forming galaxies and AGNs are easily detectable in the wavelength range 5–18 μm, even at large distances (Franceschini et al. 1991). The Canada-France Redshift Survey (CFRS) field at 1415 + 52 (Lilly et al. 1995a) is the second most observed field at all wavelengths after the Hubble Deep Field (HDF). While it does not go as deep, it is ~ 18.5 larger in area and thus is more suited for source statistics when a volume-limited ($z \leq 1$) sample is considered. It has been observed to very faint magnitudes in the $BVIK$ bands (photometric completeness down to $I_{AB} = 23.5$ mag; Lilly et al. 1995b) and possesses spectroscopic data for galaxies brighter than $I_{AB} = 22.5$ mag from the CFRS and deep radio observations ($S_{5GHz} \geq 16$ μJy; Fomalont et al. 1991). The CFRS sample can be considered complete in the sense that it contains all luminous [M_B(AB) ≤ -20.5] galaxies in the volume out to $z = 1$. This paper presents a major follow-up study of the above CFRS field, by gathering and studying representative samples of galaxies selected at radio and MIR wavelengths. With sensitivity limits of 250 μJy at 15 μm (ISOCAM) and 16 μJy at 5 GHz (VLA), these samples should include all strong and reddened starbursts up to $z = 1$ with star formation rates larger than 100 and 70 $M_\odot$ yr^{-1}, respectively. These samples should not miss any luminous FIR source in the CFRS field, as the sources were selected using observations that cover wavelengths on either side of the 60–100 μm bump. They can thus be used ultimately to estimate the star formation density that has been missed by UV flux measurements.

The nature of the μJy radio sources in the field and their optical counterparts has been extensively discussed by Hammer et al. (1995). Recently, this field has been imaged by ISOCAM in the LW2 (5–8.5 μm) and LW3 (12–18 μm) filters. We have presented the 6.75 μm LW2 observations in a previous paper (Flores et al. 1998). There we discussed the details of the data reduction, astrometry, and confidence level for each source. Fifty-four sources with a signal-to-noise ratio (S/N) ≥ 3 were detected with $S_{6.7\mu m} \geq 150$ μJy, 21 of which possess spectra from the CFRS. Of the latter, seven were stars. Among the nonstellar sources, 42% were classified as AGNs and 50% as S+A galaxies, i.e., star-forming galaxies with a significant population of A stars.

The relatively high fraction of AGNs is not unexpected, because strong AGNs are generally associated with a hot dust component and have generally bluer near-IR colors than starbursts. While the 6.75 μm data appears not to be optimal for selecting starbursts, they are useful for constraining galaxy spectral energy distributions (SEDs), as galaxies (especially Seyfert 2 galaxies) show large variations in their MIR color properties.

We present here the 15 μm LW3 observations. For galaxies in the redshift range $0.25 \leq z \leq 1$, this filter samples the 8–12 μm rest wavelength region. It can thus simultaneously provide samples of normal, starburst, and active galaxies that are complete to a well-defined bolometric flux limit (Spinoglio et al. 1995). MIR measurements are sensitive to dust thermal emission ($\lambda > 5$ μm), its broad emission being interpreted as due to polycyclic aromatic hydrocarbons (PAHs) or unidentified infrared band carriers ($3 < \lambda < 18$ μm) and nuclear nonthermal radiation. There have been recent suggestions that PAHs arise from photodissociation regions around H ɪɪ regions, the latter showing red near-IR continua (Laurent & Mirabel 1998). Genzel et al. (1997) have used the relative strengths of PAH features and near-IR colors to discriminate AGN-dominated objects from starbursts. Lutz et al. (1998) found that the fraction of AGN-powered objects is relatively small at moderate IR luminosities (typically $L_{IR} < 2 \times 10^{12}$ $L_\odot$) but reaches half at higher luminosities.

In § 2 we discuss the data reduction, astrometry and construction of the catalogs. In § 3 we present the redshift distribution of the ISOCAM LW3 objects and their optical properties, including their morphologies from *Hubble Space Telescope* (*HST*) images. Section 4 presents SEDs from UV-to-radio wavelengths and a classification scheme for these and radio-selected galaxies. Derivations of the UV and IR luminosity densities are presented in § 5. Section 6 describes the global star formation density at $z \leq 1$ and compares it with previous estimates based on the UV luminosity density.

2. OBSERVATIONS AND DATA REDUCTION

The CFRS field at 1415 + 52 was mapped with the ISOCAM LW channel (PFOV 6 arcsec pixel^{-1}) and the LW3 filter (12–18 μm). Twelve individual images were obtained using the microscanning astronomical observational template (AOT) mode (CAM01), resulting in a total integration time of ~ 1200 s pixel^{-1}. The microscanning mode provides the best spatial resolution by superposition of images. The same pixel of the sky was placed in different parts of the camera in order to minimize and detect any systematic effects. The microscanning AOT technique also allows an accurate flat-field image to be generated and yields a pixel size of 1″.5 in the final integrated image. The detection and removal of transients and glitches, integration of images, absolute flux calibration, and source detection were carried out using the method described by Désert et al. (1998). This method has been found to be particularly well adapted to our observational strategy, i.e., co-adding the 12 images without redundancy within each image. Special attention was paid to possible error propagation in the flux values. The photometric accuracy has been discussed by Désert et al. (1998). From the stellar energy distributions, we find the photometry to be accurate to a few percent for sources with S/N > 10 and to $\sim 50\%$ for sources with S/N = 3. Figure 1 displays the final 15 μm
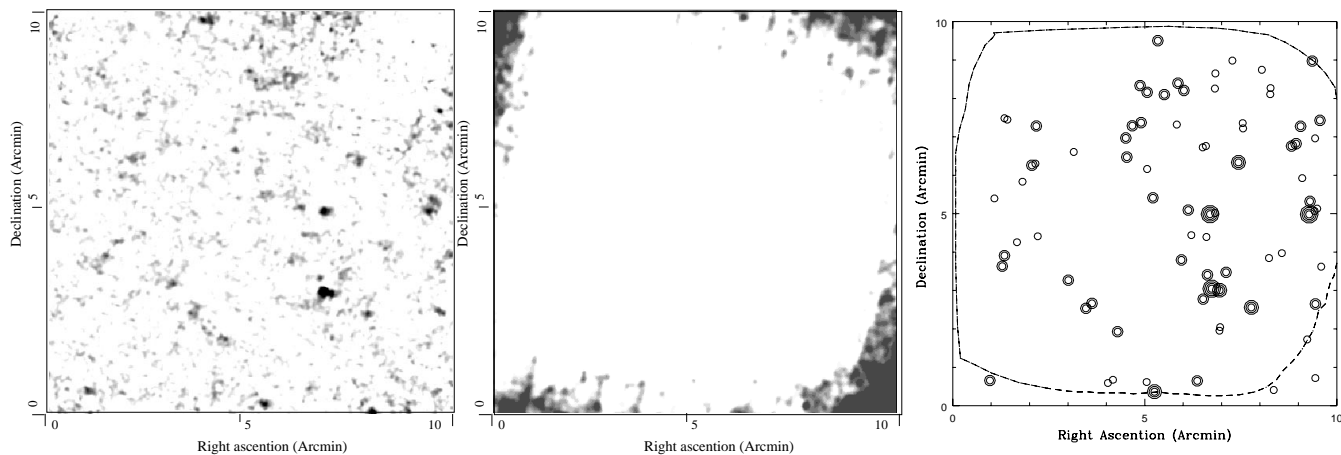
FIG. 1.—At left is the combined LW3 (12–18 μm) image of the whole 10′ × 10′ CFRS 1415 + 52 field. Center coordinates are α(2000) 14 17 53.7 and δ(2000) 52 30 30.7. The image has a FWHM resolution of ∼11″, and the scale is 1″.5 per pixel. In the middle is shown the map of noise. In 85% of the map the noise is within 10% of the average. At right are shown the locations of the cataloged 15 μm sources that have successfully passed our selection criteria (see text). Sources with S/N = 3 are represented by a single circle, while sources with S/N = 4, 6, and 8 are shown by 2, 3, and 4 concentric circles.

image of the CFRS 1415 + 52 field. Individual images were carefully registered with each other in order to optimize the image quality of the brightest compact objects (see Flores et al. 1998). The final image of the whole *ISO* field has a resolution equivalent to a median FWHM ∼ 11″ (calculated with DAOPHOT under IRAF). It can be seen that the noise structure (Fig. 1) is relatively homogeneous (the standard deviation is lower than 1/10 of the mean) in ∼85% of the area of the image, except near the edges.

Point sources are iteratively extracted with a Gaussian point-spread function (PSF) of 9″ FWHM; a correction factor of 1.39 (deduced from a detailed modeling of the effective *ISO* PSF; Césarsky et al. 1996) is applied to the measured flux (calibrated with ISOCAM user's manual conversion table) to account for losses in the wings of the true PSF.

2.1. *ISO Source Catalogs*

Source detections were made on the basis of S/N and repeatability in three independent combinations of the 12 individual images (for details about the source detection repeatability and classification, see Désert et al. 1998). The repeatability test is based on the redundancy factor, which is the number of times that the sky pixel was seen by different pixels on the camera. The software built three independent projection subrasters, and for each source candidate the flux and error are measured at the same position in each subrasters. The quality factor is based on flux measurements and varies from the best confidence index (=4) to the worst confidence level (=0; see eqs. [7]–[11] of Désert et al. 1998). We have considered only sources with a confidence level higher than 3, which means that the final source flux is within 3 σ (2 σ in the case of 4) of the source fluxes in subrasters, where σ is the error in the final source flux.

Altogether, 78 sources with S/N ≥ 3 fulfill these detection criteria (Table 1). We have considered as secure detections those sources with S/N ≥ 4 (41 sources; catalogs 1, 2, and 3). The 37 sources listed in catalogs 4, 5, and 6 with 3 < S/N < 4 are considered "less" secure. That an S/N ≥ 4 is a good detection criterion is confirmed by studies in the

Lockman Hole Deep Survey (Césarsky et al. 1998) that show that sources with S/N ≥ 4 in individual frames are confirmed in 95% of cases in the final integrated image (S/N > 10).

Figure 2 shows the flux distribution, and comparison with results from other fields suggests a completeness down to ∼350 μJy for sources with S/N ≥ 4 and to ∼250 μJy for sources with S/N ≥ 3, at least for the central 85% of the 10′ × 10′ field. These correspond to number densities of 1590 sources deg^{-2}, for $S_{15\mu m} \geq 350$ μJy, slightly larger than the number density of 1260 source deg^{-2} found by Elbaz et al. (1998) in their ISOCAM survey of the Hubble Deep Field. Surveys of low S/N ratio sources can be affected by several biases, the main ones being the possible unreli-
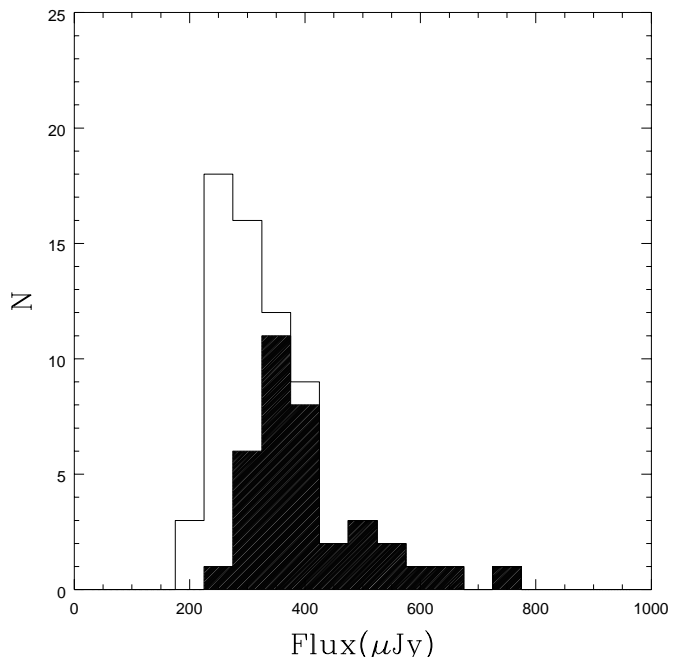

FIG. 2.—Flux distribution of ISOCAM 12–18 μm sources. Sources with S/N > 4 (catalogs 1 and 2) are shown by the shaded histogram.

TABLE 1
Optical Counterparts of ISOCAM LW3 Sources

ISO (1)	α_{2000} (2)	δ_{2000} (3)	CFRS (4)	z^a (5)	$I_{AB}^{\,b}$ (6)	$V_{AB}^{\,b}$ (7)	$K_{AB}^{\,b}$ (8)	d^c (9)	P^d (10)	Flux^e (11)	Error (12)
Catalog 1: Objects with S/N > 4, P < 0.02											
0	14:17:41.8	52:28:23.3	14.1157	1.150	20.54	22.45	...	0.65	0.000000^f	1653	57
5	14:17:41.9	52:30:23.2	14.1139	0.660	20.20	21.49	18.92	2.94	0.000383^f	562	48
9	14:17:40.4	52:28:21.1	14.1192	...	23.49	24.40	...	0.92	0.012702	399	58
13	14:17:52.0	52:25:32.8	14.0855	...	20.92	22.60	...	0.72	0.000998	487	69
32	14:17:56.6	52:31:58.6	14.0711	...	21.44	22.29	20.26	1.50	0.006552	274	54
42	14:18:20.9	52:25:53.0	14.0098	star	14.66	16.44	...	1.53	0.000029	362	69
43	14:17:42.6	52:28:46.3	14.1129	...	21.05	22.35	20.30	0.57	0.000694	209	52
44	14:17:34.9	52:27:51.0	14.1329	0.375	19.52	20.60	...	1.89	0.000294^f	347	52
51	14:17:24.3	52:30:24.0	14.1567	0.479	19.79	20.04	18.62	2.99	0.006937	459	57
84	14:17:45.8	52:30:31.2	14.1028	0.988	21.57	23.84	19.69	1.52	0.007463^f	295	50
145......	14:18:07.1	52:28:37.3	14.0446	...	20.00	21.33	...	0.31	0.000089	314	54
206......	14:18:13.4	52:31:47.3	14.0272	0.668	20.51	21.70	19.12	1.51	0.003157	297	55
233......	14:17:58.5	52:27:14.8	14.0663	0.743	20.88	22.34	...	2.51	0.002081	288	56
282......	14:18:18.9	52:29:05.4	14.0138	star	15.77	16.80	15.43	5.66	0.000985	214	53
294......	14:17:47.0	52:29:11.9	14.0998	0.430	20.58	21.84	19.06	2.44	0.008694^f	245	53
303......	14:17:46.4	52:33:50.8	14.1006	...	20.66	21.74	...	2.12	0.007003	270	53
308......	14:17:26.7	52:32:20.9	14.1511	...	20.71	21.61	...	0.78	0.000990	284	61
369......	14:18:4.0	52:27:47.6	14.9154	0.812	21.57	23.06	...	3.25	0.000489^f	304	51
Catalog 2: Objects with S/N > 4, P(d, I) > 0.02											
8	14:17:23.8	52:27:49.3	14.1598	...	19.84	21.00	...	8.87	0.061772	367	73
24	14:17:23.7	52:34:33.7	14.1582	...	22.78	23.44	...	3.92	0.123123	341	77
138......	14:17:26.3	52:32:51.5	14.1527	...	23.00	24.24	...	5.54	0.268762	252	62
139......	14:18:18.3	52:29:16.3	14.0150	...	22.23	24.19	19.98	1.64	0.014691	284	57
160......	14:17:37.4	52:31:41.9	14.1278	...	22.08	28.36	20.31	11.04	0.448282	401	55
190......	14:17:54.1	52:33:56.2	14.0779	0.578	22.01	23.10	...	2.94	0.039091	255	53
195......	14:17:24.6	52:30:40.1	14.1569	...	20.61	21.65	19.51	7.05	0.071948	364	61
258......	14:17:41.1	52:30:22.3	14.1166	1.015	22.46	23.88	20.46	5.24	0.166123	188	47
258......			14.1178	9.999	22.47	24.66	20.24	6.38	0.237751	188	47
278......	14:17:42.9	52:28:00.8	14.1103	0.209	22.33	22.64	...	7.84	0.306807	235	55
278......			14.1145	...	22.64	25.72	...	7.72	0.365875	235	55
278......			14.1091	...	22.02	22.79	...	10.70	0.412821	235	55
278......			14.1125	...	22.62	25.75	...	8.45	0.415531	235	55
296......	14:17:56.0	52:32:55.9	14.0741	...	23.00	23.16	...	6.09	0.314943	207	49
296......			14.0743	...	21.65	22.74	...	10.58	0.320898	207	49
304......	14:17:27.3	52:32:09.6	14.1489	...	20.91	20.54	...	9.14	0.147525	284	61
307......	14:17:47.9	52:34:06.6	14.0975	...	21.21	23.19	...	7.45	0.126166	252	55
325......	14:18:12.5	52:32:48.4	14.0291	...	22.19	24.51	...	3.88	0.077093	225	51
361......	14:17:49.9	52:33:43.2	14.0909	0.978	22.34	24.30	...	2.12	0.026649	248	56
372......	14:18:02.7	52:27:59.6	14.0557	...	21.63	22.51	...	3.57	0.042434	225	52
421......	14:17:52.5	52:35:13.4	14.9907	...	22.95	19.41	...	7.78	0.447372	259	55
434......	14:17:44.1	52:25:50.5	14.1070	...	20.86	21.33	...	5.82	0.060281	277	65
440......	14:17:39.3	52:28:46.1	14.1232	...	22.06	23.19	20.05	3.91	0.070782	245	55
440......			14.1212	...	20.20	20.65	20.30	8.87	0.081572	245	55
457......	14:17:52.1	52:30:49.8	14.0846	0.989	21.81	23.15	20.34	2.97	0.034073	250	50
Catalog 3: Objects with S/N > 4, without optical counterpart in I_{AB}											
021......	14:17:23.2	52:32:58.3	...	...	...	...	...	...	1.0000000	270	62
202......	14:17:57.3	52:32:29.8	...	...	...	...	...	...	1.0000000	209	49
288......	14:17:53.6	52:33:44.6	...	...	...	...	...	...	1.0000000	231	55
439......	14:17:54.7	52:32:54.9	...	...	...	...	...	...	1.0000000	248	53
Catalog 4: Objects with 4 > S/N > 3, P < 0.02											
171......	14:18:16.1	52:29:39.2	14.0198	1.603	20.04	20.21	19.86	1.52	0.002196	211	56
183......	14:17:30.9	52:33:44.0	14.1400	star	15.61	16.13	...	5.59	0.000845	208	60
228......	14:17:23.3	52:30:33.4	14.1609	star	18.93	20.83	18.30	2.54	0.002518	193	61
243......	14:17:35.9	52:32:46.6	14.1302	0.548	20.85	21.72	...	3.19	0.018359	188	55
310......	14:18:15.0	52:31:22.2	14.0227	0.772	20.84	22.08	19.47	3.42	0.020906	196	53

TABLE 1—*Continued*

ISO (1)	α_{2000} (2)	δ_{2000} (3)	CFRS (4)	z^a (5)	$I_{AB}{}^b$ (6)	$V_{AB}{}^b$ (7)	$K_{AB}{}^b$ (8)	d^c (9)	P^d (10)	Flux^e (11)	Error (12)
326	14:17:53.5	52:25:51.5	14.0818	0.899	21.02	22.14	...	2.74	0.010601	165	54
351^g......	14:17:40.7	52:33:57.9	14.9504	...	23.90	99.99	...	8.44	0.005986^f	228	59
354	14:17:47.8	52:32:52.8	14.0968	...	23.39	24.88	...	1.07	0.015834	172	54
396	14:18:18.2	52:33:04.9	14.0151	...	17.92	18.19	...	1.93	0.000647	185	53
408	14:17:40.5	52:27:14.7	14.1190	0.754	20.99	22.49	...	0.95	0.001837^f	185	56
427	14:17:59.7	52:26:01.4	14.0645	...	22.44	24.40	...	9.72	0.000824^f	247	67
449	14:17:42.7	52:32:21.6	14.1117	...	20.79	21.15	...	3.77	0.024364	213	54
475	14:17:53.9	52:31:37.0	14.0820	0.976	21.69	24.27	19.37	11.82	0.012867^f	203	53
Catalog 5: Objects with $4 >$ S/N > 3, $P > 0.02$											
137	14:17:23.9	52:25:54.1	14.1597	...	23.05	25.95	...	4.89	0.224187	284	93
174	14:17:45.3	52:29:47.6	14.1042^a	0.722	21.49	23.38	19.79	3.67	0.040133	197	50
183	14:17:30.8	52:33:54.2	14.1403	...	21.48	24.21	...	4.96	0.071532	208	60
228	14:17:23.7	52:30:29.7	14.1591	...	22.76	23.65	21.60	5.51	0.225442	193	61
243	14:17:36.0	52:32:55.4	14.1300	...	23.25	24.15	...	5.65	0.328192	188	55
276	14:18:12.7	52:31:41.8	14.0287	...	22.29	24.19	19.98	7.56	0.281069	175	51
277	14:17:24.7	52:26:56.2	14.1554	...	21.90	23.07	...	5.51	0.120360	240	76
341	14:17:23.9	52:32:28.0	14.1576	...	22.33	23.83	...	9.93	0.444487	214	64
341			14.1596	...	24.21	26.44	...	4.52	0.422721	214	64
367	14:17:25.7	52:31:32.2	14.1533	...	22.42	23.19	21.81	7.46	0.299945	177	54
377	14:17:40.8	52:34:13.0	14.1170	...	21.83	23.92	...	5.14	0.100134	233	60
384	14:17:42.6	52:29:54.3	14.1120	...	22.60	23.57	20.78	6.25	0.251090	187	51
396	14:18:17.7	52:33:02.6	14.0157	...	22.35	23.01	...	7.03	0.258736	185	53
399	14:18:05.8	52:32:10.2	14.0477	...	23.01	24.73	...	4.36	0.177522	179	53
408	14:17:40.3	52:27:20.6	14.1195	...	22.67	24.42	...	5.85	0.235036	185	56
424	14:18:12.3	52:29:45.4	14.0302	...	20.87	22.20	19.22	5.07	0.046449	191	50
426	14:18:19.9	52:30:47.2	14.0112	...	23.53	24.86	20.61	6.04	0.433874	160	53
442	14:17:38.5	52:34:43.2	14.1252	...	21.91	21.79	...	10.02	0.347868	221	69
449	14:17:43.3	52:32:19.5	14.1100	...	24.46	24.37	...	2.75	0.220019	213	54
474	14:17:31.7	52:29:11.0	14.1393	...	22.23	23.67	21.28	2.42	0.031712	160	52
Catalog 6: Objects with $4 >$ S/N > 3, without optical counterpart in I_{AB}											
231	14:17:33.4	52:34:21.1	...	...	...	...	...	...	1.0000000	209	59
268	14:17:31.4	52:25:37.5	...	...	...	...	...	...	1.0000000	224	70
348	14:18:06.3	52:25:32.0	...	...	...	...	...	...	1.0000000	193	67
359	14:17:23.0	52:28:59.2	...	...	...	...	...	...	1.0000000	234	73
483	14:17:29.9	52:29:21.3	...	...	...	...	...	...	1.0000000	167	53

^{a} The redshift for 14.1042 was given as $z = 0.7217$ by Lilly et al. (1995b). Redshifts for the four stars (denoted by "star") were determined from additional spectra. An ellipsis indicates that the redshift is unknown.
^{b} An ellipsis indicates that the magnitude is not available.
^{c} Distance in arcseconds between *ISO* source and optical or radio counterpart.
^{d} Probability that the coincidence is by chance.
^{e} Flux within a 9″ aperture in μJy not corrected for aperture effects (see text).
^{f} Radio source with probability based on radio-source counts.
^{g} Hammer et al. (1995) and Fomalont et al. (1992) comment that the fainter source ($I_{AB} \sim 23.9$) galaxy, which is 2″ away, should be the optical counterpart. Unfortunately, no spectrum of the fainter galaxy is available.

ability of sources near the survey limit and Eddington bias. Near the flux density limit, completeness falls off, and possible false sources may be introduced. The fraction of false sources can be controlled through a random match control test based on the identification rate of ISOCAM sources with optical sources (see next section) and should be small. We have checked whether our higher number count relative to the HDF data could be due to the Eddington bias. Our survey is intermediate in depth between the Lockman Hole Deep Survey (from 450 to 1400 μJy) and HDF survey (from 125 to 350 μJy). Elbaz et al. (1998) quote a slope of 1.3 and 2.1 for the HDF and Lockman Hole, respectively, and we should expect an intermediate slope near ~ 1.7, lower than the value of 2.2 derived from our $S \geq 250$ and $S \geq 350$ μJy counts. We have attempted to estimate the fraction of sources that may have entered our sample erroneously because statistical uncertainties bring them over the detec-

tion threshold, while they actually possess a lower flux density than $S = 250$ μJy. We have adopted a slope of 1.7 and perform Monte Carlo simulations of 30,000 sets, assuming a Gaussian distribution for the noise of faint sources. The simulations show that $\sim 15\%$ of the sources with S/N ≥ 3 can be sources with fluxes lower than 250 μJy, but that fraction drops to only $\sim 2\%$ for sources with S/N ≥ 4. This is probably close to the truth, since after accounting for the Eddington bias (i.e., removing 15% of the 78 sources with S/N > 3 as well as 2% of the 41 S/N > 4 sources), the slope becomes 1.7, in good agreement with other surveys.

Biases in source counts thus affect mainly the faintest sources in our sample (those with $3 \leq$ S/N < 4). They are the least powerful sources and as such cannot introduce significant uncertainties on global luminosity density estimates.

2.2. *Astrometry and Counterparts at Radio and Optical Wavelengths*

The positional accuracy of *ISO* sources is affected by both the pixel size and distortion (see Flores et al. 1998). The superposition of the ISOCAM field onto the CFRS 1415+52 optical field was done by matching the positions of the six brightest sources (which were also detected at 6.75 μm). By comparing the astrometry of the optical and ISOCAM LW3 sources, we find a median difference of $\sim 3''.7$. This is reasonable given that the *ISO* pixel size is $\sim 6''.0$.

The astrometric accuracy of the CFRS 1415+52 optical field is $0''.15$, based on the comparison between the optical and radio frames (Hammer et al. 1995). We first compare the 15 μm image with the VLA μJy radio map (Fomalont et al. 1991) and calculate the probability of a pure coincidence, assuming Poisson statistics:

$$P(d, S_{5\,\text{GHz}}) = 1 - e^{-n(S_{5\,\text{GHz}})\pi d^2} ,\qquad (1)$$

where d is the angular distance between the ISOCAM LW3 source and the radio source in degrees and n is the integrated density of radio sources with flux $S_{5\text{GHz}}[dn(S_{5\text{GHz}}) = 83520 S_{5\text{GHz}}^{-1.18} dS]$. Ten ISOCAM LW3 sources are thus identified (see Table 1). They all possess optical counterparts (Hammer et al. 1995).

Astrometry of ISOCAM LW3 sources not detected in radio has been derived by comparison with the optical sources in the CFRS 1415+52 field, and

$$P(d, I_{AB}) = 1 - e^{-n(I_{AB})\pi d^2}\qquad (2)$$

is the probability of a pure coincidence, where $n(I_{AB})$ are integrated counts derived from the CFRS. In Table 1, six catalogs have been defined with different S/N ($3 \leq S/N \leq 4$, $S/N > 4$) and P values ($P < 0.02$, $P > 0.02$, and sources without optical counterparts within $12''$). Objects that are also radio sources are indicated. These all have very low probabilities of accidental coincidence.

We also compare the 15 μm map with that described in Flores et al. (1998) at 6.75 μm. We found 17 of the 78 15 μm sources to also be detected at 6.75 μJy (with flux densities above 150 μJy). The fraction of 15 μm sources also detected at 6.75 μm increases with S/N (see Table 2).

The final noise structure in ISOCAM images is not strictly Gaussian because of possible residuals glitches and because the 15 μm positions could not have been fully corrected for image distortions. To calibrate the probabilities given in Table 1 in an empirical way, we have applied a random match control test to the ISOCAM image by rotating it successively by 45°, 90°, 180°, and 270° relative to the

optical image. Only 3 ± 1 of the 78 ISOCAM sources were found to be randomly associated with an optical counterpart with $I_{AB} < 22.5$ and $P < 0.02$. This should be compared with the 37 $I_{AB} < 22.5$ and $P < 0.02$ counterparts found in Table 1. These experiments suggest that non-Gaussian effects cannot affect our probability calculations by more than a factor of 2.

Table 1 lists the sources in six catalogs, the confidence level decreasing in each successive catalog. The ISOCAM LW3 sources and their optical counterparts are given in columns (1) and (2). Column (3) provides the optical source redshift when available, a star indicates that the *ISO* source is stellar, while an ellipsis indicates that no redshift is available. Columns (4), (5), and (6) are the *I*, *V*, and *K* isophotal magnitudes in the AB system, and an ellipsis indicates that no photometry is available. Column (7) gives the angular distance in arcsec between the ISOCAM LW3 source and optical (or radio) identification, while column (8) gives the associated probability of coincidence. Columns (9) and (10) give the flux density at 12–18 μm and its error in μJy. The positions and flux densities of the nine nonidentified *ISO* sources are also listed in Table 1 (catalogs 3 and 6).

Among the sources with $S/N \geq 4$, only eight (19%) have counterparts fainter than $I_{AB} = 22.5$ or no optical counterparts. These sources could be at redshifts higher than 1. The fraction of very faint optical counterparts increases for the fainter ISOCAM LW3 sources (41% for sources with $3 < S/N < 4$), which is to be expected. On the other hand, in the most uncertain catalog (catalog 5) one can expect ~ 4.6 sources out of 19 to be pure coincidental projection. In seven cases, more than one optical counterpart appear to be related to an ISOCAM LW3 source. In the following analyses, we have used the "best" optical identification (i.e., those with lowest coincidental probability), but in Table 1 we have listed all possible optical identifications with a probability within a factor of 2 of the smallest probability.

3. OPTICAL PROPERTIES OF THE 15 μm COUNTERPARTS

3.1. *Color and Redshift Distributions*

The $(I - K)_{AB}$ color distribution of the 15 μm optical counterparts (Fig. 3) is significantly redder than that of the CFRS survey (top panel), with a median 0.5 mag redder than that of CFRS galaxies $[\langle (I - K)_{AB}\rangle \sim 1.3]$.

Twenty-six of the sources detected at 15 μm and with $I_{AB} \leq 22.5$ have spectroscopy available in the CFRS database. Among these are four stars that are also detected at 6.75 μm. Figure 4 shows the redshift histogram of *ISO* sources superposed on the CFRS redshift distribution. The median redshift value of the ISOCAM LW3 galaxies ($\langle z\rangle \sim 0.76$) is higher than that of the CFRS ($\langle z\rangle \sim 0.58$) but coincides with that of the $S_{5\text{GHz}} \geq 16$ μJy radio sources (Hammer et al. 1995). Since 70% of the 15 μm optical sources have $I_{AB} \leq 22.5$, we estimate from the redshift distribution that more than 63% of the sources with $S_{15\mu m} \geq 250$ μJy are at $z \leq 1$.

3.2. *Spectral Classifications*

The spectrophotometric classification of the 15 μm optical counterparts is based on optical and emission-line properties using diagnostic diagrams and spectral templates (see Hammer et al. 1995, 1997). The following spectrophotometric types are found: 15 emission-line galaxies,

TABLE 2

COUNTS OF *ISO* CATALOGS AT 15 μm

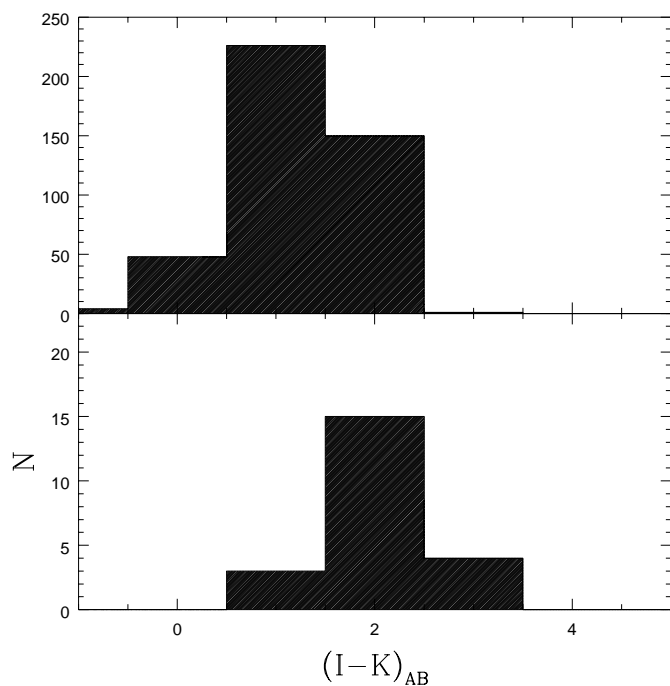|	S/N ≥ 4	4 > S/N ≥ 3	S/N ≥ 3
Total	41	37	78
Number $I_{AB} \leq 22.5$	33	22	55
With z	17	9	26
Number $I_{AB} > 22.5$	4	10	14
No id	4	5	9
LW2 detection	10	7	17
radio detection	5	5	10[a]

[a] Radio sources with $SS_{5\text{GHz}} \geq 16$ μJy.

FIG. 3.—$(I-K)_{AB}$ color distribution of 15 μm sources with $I_{AB} \leq 22.5$ (*bottom panel*) compared with the CFRS galaxy color distribution (*top panel*).

three active galaxies (including the QSO CFRS 14.0198 at $z = 1.6$, the most distant CFRS object), one quiescent galaxy, one spiral galaxy, and one H II galaxy (CFRS 14.1103). Figure 5 shows the spectra of all extragalactic objects classified by their spectrophotometric type.
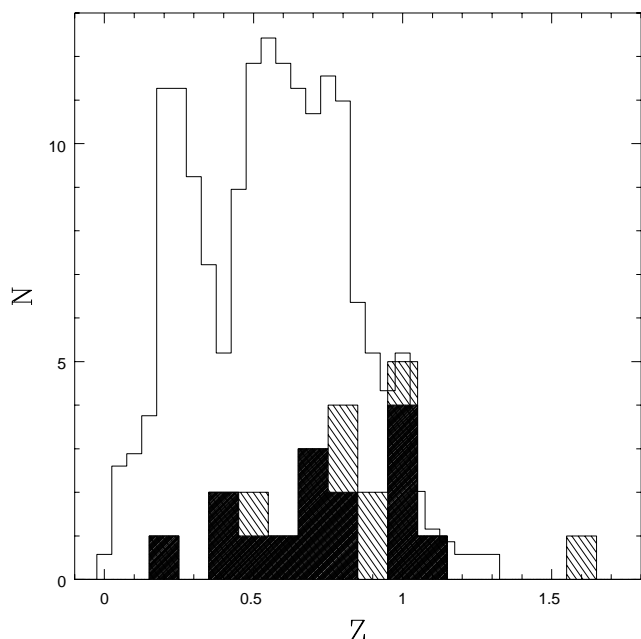

FIG. 4.—Dashed histogram shows the redshift distribution of the 22 identifications with spectra found in the CFRS database. The shaded histogram shows the redshift distribution of the sources in the catalogs 1 and 2. The unshaded histogram shows the CFRS redshift distribution after rescaling.

Most (71%) of the 15 μm optical counterparts are classified as S+A galaxies, which are galaxies with moderate [O II] emission ($W_{[O II]} \sim 20$ Å) and characterized by large $D(3550\text{-}3850)$ indices (see Table 3), as defined in Hammer et al. (1997). Large $D(3550\text{-}3850)$ values can be caused by either a large A star population [$D(3550\text{-}3850)$ is correlated with the Hδ equivalent width, $D(3550\text{-}3850)=0.2$, corresponding to $W(H\delta) = 5\text{-}7$ Å for a nonextincted galaxy] or very large extinctions. As we shall see, it is the A star hypothesis that is the most plausible. This suggests that in most extragalactic 15 μm sources there was star formation occurring about 0.5 Gyr prior to the observed event. The importance of the S+A population is also supported by the fact that at high redshift, galaxies with large $D(3550\text{-}3850)$ are also detected at 6.75 μm and 1.44 GHz.

3.3. *Morphologies from HST and CFHT*

About 30% of the CFRS field at 1415+52 has been observed by the *HST*. Public domain *HST* images of objects in the CFRS and Autifib/Low Dispersion Survey Spectrograph survey (Brinchmann et al. 1997) and Groth Survey (Groth et al. 1994) are available. Among the 55 $I \leq 22.5$ *ISO* sources with optical counterparts, 16 (30%) with have been observed with the *HST* F814W filter. *HST* images of optical counterparts of μJy radio sources can be find in Hammer et al. (1996).

Figure 6 displays a mosaic of *HST* images of optical counterparts with $I_{AB} \leq 22.5$ of 15 μm sources. For each source the CFRS name is indicated, as well as its morphological classification, by either Brinchmann et al. (1997) or us.

Two sources are unresolved by the *HST* (one QSO and one H II region, 14.1103). Six galaxies (37%) are found in strongly interacting systems, four (25%) are E/S0 galaxies, and four (25%) are disk-dominated galaxies. Most of the 14 resolved sources show irregularities that might be interpreted as pre- or postmerging events.

4. SPECTRAL ENERGY DISTRIBUTIONS AND OBJECT CLASSIFICATIONS

4.1. *SEDs of Local Galaxies: Toward A Template Database*

Several groups have been gathering multiwavelength observations of local galaxies (Spinoglio et al. 1995; Schmitt et al. 1998). The main limitations of the data sets are the assumed aperture corrections and possible AGN variability. SEDs of galaxies in the same class often show large differences, especially in the infrared. This is especially true for Seyfert 2 galaxies, which show a wide range of colors in the near- and far-IR (Spinoglio et al. 1995). This large dispersion motivated us to use mean SEDs of local galaxies to compare with distant sources so as to avoid biases for or against a given class of galaxies. For example, some Seyfert 2 galaxies may be misclassified as starbursts, but the effect on global quantities would be compensated by true starburst galaxies that are misclassified as Seyfert 2 galaxies. However, average properties can be affected by a single object with extreme properties. For example, in the Schmitt et al. (1998) sample, the average radio luminosities for elliptical and spiral galaxies appears to be overestimated because of the large radio powers of NGC 1316 and NGC 598, respectively. Indeed, the mean values are significantly (~ 8 times) larger than those derived from the much larger and more complete sample of local ellipticals of Wrobel &
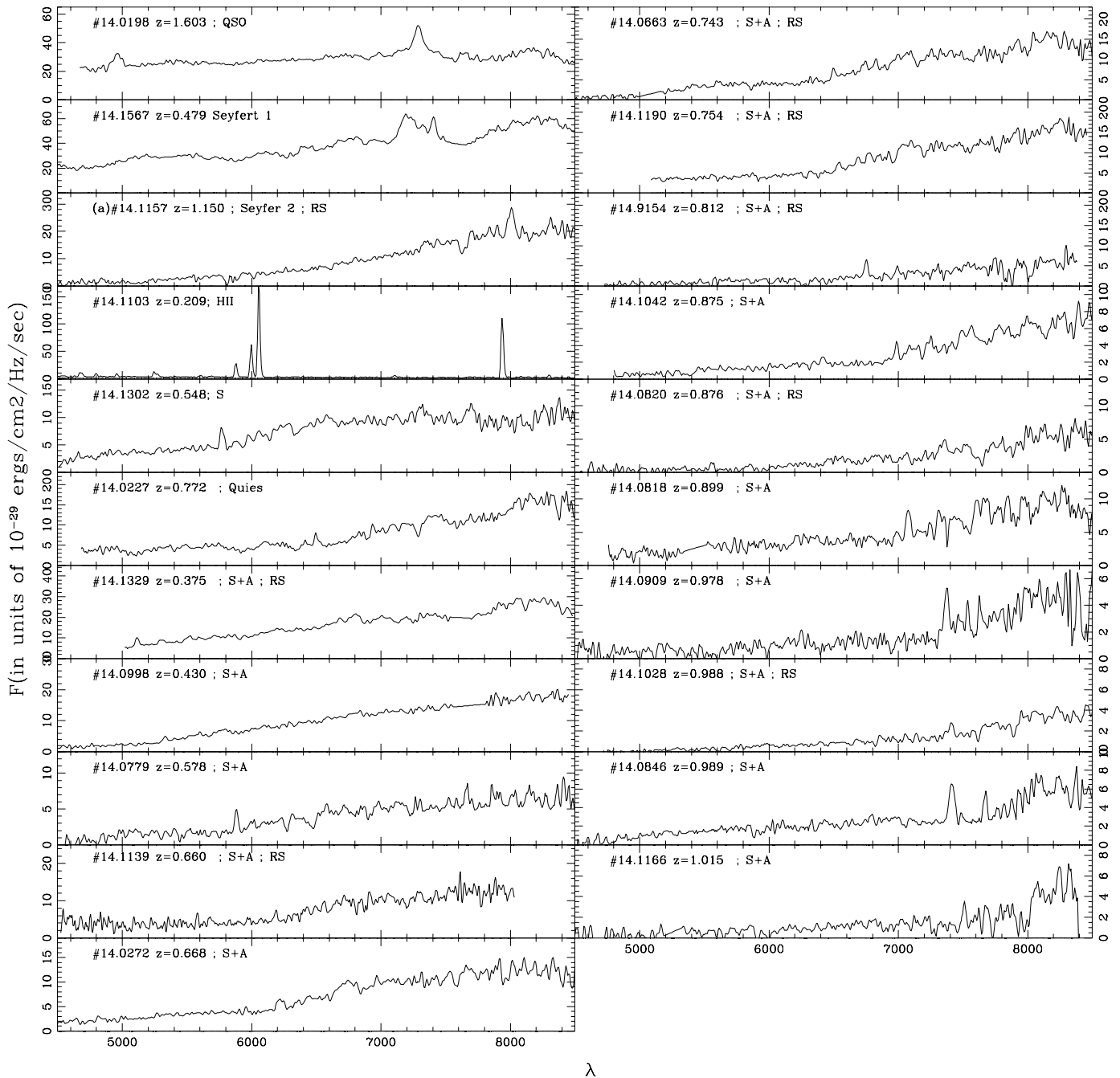
Fig. 5.—Spectral classification of the 21 15 μm sources with available spectra according to their continuum and line properties. For each object the CFRS name, redshift, and spectral classification are given in the upper left corner.

Heeschen (1991). Using the median rather than the mean would provide a value in much closer agreement with Wrobel & Heeschen and an SED for spirals that follows the radio-FIR correlation (Condon 1992). In the following we will use only median points for determining the SED of local templates.

Another concern is whether using local templates to analyze the properties of distant sources is appropriate. We have compared the two samples of local galaxies that have been classified and studied at several wavelengths. The Schmitt et al. sample has been mainly selected from the *IUE* archives and the Spinoglio et al. sample from the 12 μm faint IRAS catalog. Our 15 μm sample has been selected at the wavelengths $15/(1 + z)$ and $0.835/(1 + z)$ μm so that

both local samples are a priori appropriate for use as templates for our sources. The two local samples show somewhat different properties in their SEDs, especially concerning the average IR properties of Seyfert 2 galaxies. The Schmitt et al. galaxies are bright infrared galaxies and include most of the starburst and AGN templates used by Genzel et al. (1998) to compare with ultraluminous IRAS galaxies. Conversely, the Spinoglio et al. sample includes galaxies varying over a 4–5 mag range of luminosities in the infrared, and their average SEDs are mostly dominated by fainter galaxies. Figure 7 shows the distribution of luminosities for the VLA/ISOCAM/CFRS objects. Rest frame luminosities at 7 μm have been interpolated from broadband observations at 0.835, 2.2, 6.75, and 15 μm and are

TABLE 3

χ^2 VALUES FOR ALL GALAXIES OF THE 15 μm AND RADIO SAMPLES AND CLASSIFICATIONS

| CFRS	E		Sp		LINER		Seyfert 2		SBL		SBH		Hybrid			Class
	χ^2	Error	χ^2	Error	χ^2	Error	χ^2	Error	χ^2	Error	χ^2	Error	χ^2	Error	Percent SBH + Percent S	
14.0227......	12.69	1.24	3.18	0.59	2.47	0.81	0.97	0.27	2.21	0.78	0.37	0.31	0.19	0.13	9+1	SB+S
14.0272......	12.11	1.69	4.45	0.93	2.54	0.88	1.16	0.45	1.58	0.60	0.41	0.32	0.29	0.20	8+2	SB+S
14.0276......	4.22	0.31	0.75	0.22	0.75	0.18	0.51	0.17	4.10	0.85	1.32	0.20	0.15	0.12	8+2	SB+S
14.0573......	...	...	...	...	...	...	...	...	...	...	...	...	...	...	...	Seyfert 1
14.0663......	8.11	0.61	1.51	0.70	1.58	0.26	0.59	0.04	2.18	0.84	0.47	0.06	0.51	0.10	9+1	SBH
14.0727......	11.90	0.95	4.07	1.25	2.89	0.38	1.41	0.30	0.70	0.30	0.55	0.16	0.23	0.19	8+2	SB+S
14.0779......	16.16	2.25	21.11	18.57	6.07	1.31	0.55	0.17	1.73	0.54	0.63	0.30	1.40	0.67	9+1	Seyfert 2 /SBH
14.0818......	13.20	0.89	3.0	60.15	4.10	0.54	1.17	0.22	2.27	2.17	0.48	0.32	0.23	0.11	8+2	SB+S
14.0820......	2.94	2.21	0.62	0.19	1.69	1.85	2.13	0.22	16.92	4.31	6.59	0.99	0.64	0.26	1+9	S
14.0846......	8.94	0.74	2.17	0.22	3.65	1.16	0.45	0.19	4.85	3.24	0.83	0.29	0.35	0.22	4+6	SB+S /Seyfert2
14.0854......	3.46	0.43	0.73	0.22	0.94	0.40	0.21	0.10	6.47	1.27	1.42	0.11	0.06	0.13	8+2	SB+S /Seyfert2
14.0909......	5.13	0.97	1.51	0.33	1.55	0.24	0.15	0.01	6.36	1.05	1.67	0.21	1.46	0.56	4+6	Seyfert 2
14.0937......	15.61	9.20	3.63	0.72	10.81	4.20	1.53	0.16	12.68	6.98	8.53	3.37	2.79	1.11	1+9	Seyfert 2
14.0998......	7.89	1.75	4.42	4.22	1.42	0.19	0.86	0.18	2.92	0.23	0.51	0.22	0.31	0.20	6+4	SB+S
14.1028......	3.13	0.43	0.86	0.31	0.66	0.16	0.25	0.12	6.23	0.41	1.47	0.15	0.54	0.24	4+6	Seyfert 2 /SB+S
14.1041......	23.07	6.23	33.67	72.26	6.21	1.72	1.45	0.11	1.59	0.93	7.34	3.11	1.81	1.08	8+2	Seyfert 2 /SB+S
14.1042......	8.29	0.75	3.01	1.18	1.43	0.16	0.45	0.13	4.01	0.25	0.95	0.18	0.38	0.15	8+2	SB+S /Seyfert2
14.1103......	...	...	...	...	...	...	...	...	...	...	...	...	...	...	...	H II
14.1129......	13.09	2.76	2.77	0.63	3.53	1.99	0.97	0.47	1.23	0.70	0.54	0.28	0.49	0.31	7+3	SB+S
14.1139......	8.83	0.24	2.05	0.12	1.69	0.09	0.66	0.08	1.36	0.05	0.28	0.06	0.81	0.07	9+1	SBH
14.1190......	8.57	0.79	1.34	0.27	1.59	0.58	0.80	0.21	2.01	0.94	0.37	0.17	0.45	0.13	9+1	SBH
14.1302......	...	...	...	...	...	...	...	...	...	...	...	...	...	...	...	Seyfert 1
14.1303......	...	...	...	...	...	...	...	...	...	...	...	...	...	...	...	QSO
14.1329......	18.24	1.11	8.25	0.13	3.01	0.11	3.29	0.10	3.47	0.14	2.91	0.42	4.62	0.63	9+1	SBH /Seyfert2
14.1567......	...	...	...	...	...	...	...	...	...	...	...	...	...	...	...	Seyfert 1
14.9025......	...	...	...	...	...	...	...	...	...	...	...	...	...	...	...	LINER
14.9154......	25.58	0.27	6.54	0.18	12.43	0.23	1.52	0.08	12.15	0.23	5.43	0.12	5.47	0.19	4+6	Seyfert 2
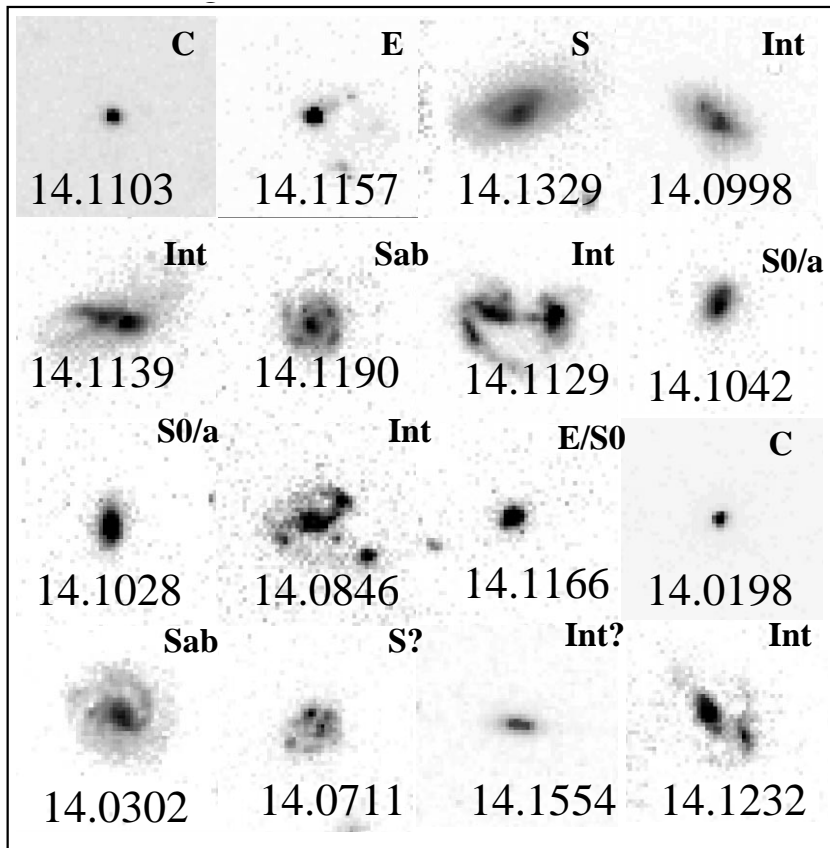
FIG. 6.—*HST* 5″ × 5″ images obtained with the F814W filter of 16 sources detected at 15 μm with $I_{AB} < 22.5$. For each galaxy the morphological classification is given in the upper right corner.

available for most objects, except those detected only at radio wavelengths. At $z \geq 0.5$ these galaxies have luminosities comparable with those of the Schmitt et al. galaxies and are 1.5–2.5 mag brighter than the mean magnitude of the Spinoglio et al. galaxies. It is reasonable to think that the discrepancies at IR wavelengths between the Spinoglio et al. and Schmitt et al. galaxies are mainly due to the large IR luminosity differences. The large dispersions displayed by individual Schmitt et al. galaxies in each class (especially for Seyfert 2 galaxies) ensure that this local sample is the most appropriate one for comparison with the intrinsically bright distant galaxies.

4.2. *Classifications of the 15 μm Radio Galaxies from Their SEDs*

According to Schmitt et al. (1997), the UV-to-optical range constitutes the best discriminator between Seyfert 2 and SBH or SBL (starburst with low extinction) galaxies. Seyfert 2 galaxies are generally early-type spirals, with UV colors typically bluer than those of spirals (see, e.g., Kennicutt 1992). Figure 8 shows the color distribution of the radio–15 μm samples. In the ($B-K$, 2800 Å − B) diagram, their colors are reasonably well fitted by Bruzual & Charlot (1995) models, except for three objects that are either QSOs or Seyfert 1 galaxies. They display a range of colors that are well fitted by starburst and spiral templates. The same conclusion can be drawn from the ($B − 7$ μm, 2800 Å − B) diagram, with a few objects having $B − 7$ μm colors consistent with those of Seyfert 2 templates. The latter are likely to be associated with hot dust and have redder optical-MIR colors than starbursts. In summary, most of the galaxies
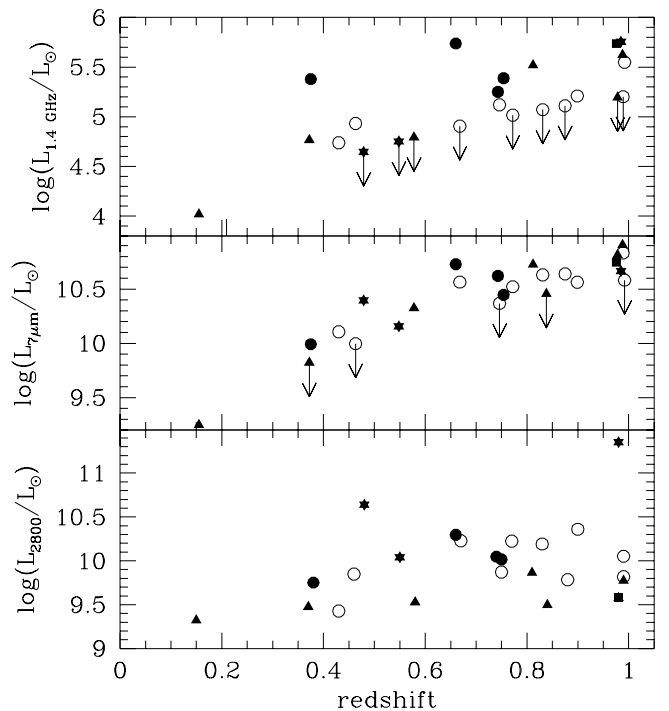
FIG. 7.—Logarithm of the luminosities at rest, 1.4 GHz, 7 μm, and 2800 Å against redshift. Rest frame luminosities have been interpolated from the observed luminosities at 1.4 and 5 GHz, at 0.835, 2.2, 6.75, and 15 μm, and at 8350, 5500, and 4350 Å, respectively. Filled dots represent SBH, open dots S + SBH, triangles Seyfert 2 or LINER, and stars QSO or Seyfert 1. Vertical arrows indicate a detection limit.
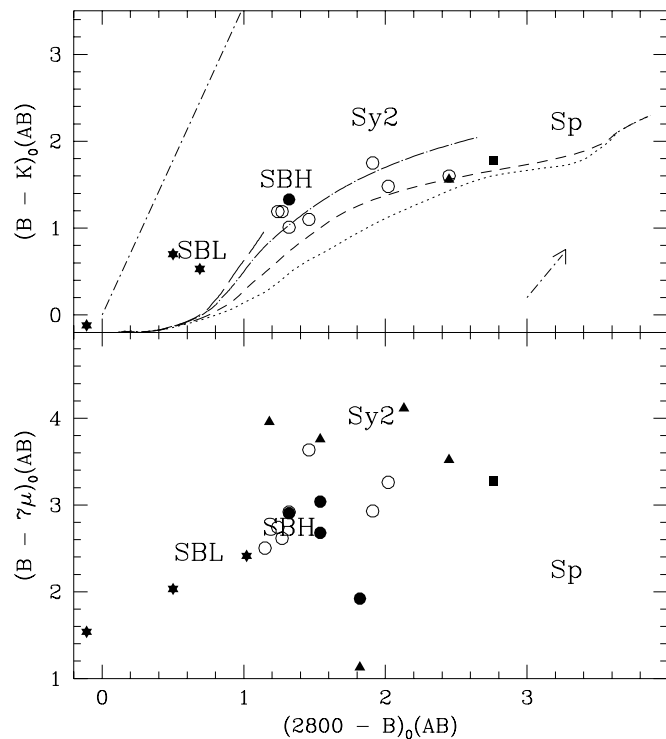
FIG. 8.—Color-color diagrams for the 15 μm and radio sources. The symbols have the same meaning as in Fig. 7. In the top diagram are represented galaxies with *K*-band photometry. In the bottom diagram galaxies without IR measurements are excluded. In the top diagram are shown stellar tracks from Bruzual & Charlot (1995; *top to bottom*, exponentially decreasing SFR, with τ = 4, 1, and 0.5 Gyr, respectively). The dash-dotted lines represent a power law, and the extinction vector is indicated. In both diagrams are shown the color-color location of Schmitt et al. (1998) galaxy templates.

detected at 15 μm have colors from the UV to MIR consistent with those of star-forming objects: starburst and spiral galaxies.

SEDs for the 27 extragalactic 15 μm radio sources with $z \leq 1$ have been constructed using the observed fluxes at visible (B_{AB}, V_{AB}, and I_{AB} magnitudes), near-IR (K_{AB} when available), MIR (6.75 μm, Flores et al. 1998; 15 μm, Table 1), and radio wavelengths (1.4 and 5 GHz from Fomalont et al. 1991) and shifted to rest wavelengths. Each SED has then been compared with the average SED of well-known local objects (a sample of 59 galaxies; Schmitt et al. 1997). The latter include E (ellipticals), Sp (spirals), SBHs, SBLs, Seyfert 2 galaxies, and LINERs. Schmitt et al. (1997) also provided standard deviations of the mean, which allows us to optimize the comparison.

In order to classify the SEDs, we have performed Monte Carlo simulations, assuming independent variations of our flux measurements within Gaussian error bars. In each of the 5000 Monte Carlo sets, every object SED has been fitted to template SEDs spanning all the classes defined by Schmitt et al, providing a χ^2 value weighted by the standard deviations of the mean given by those authors. Because galaxies often show properties intermediate between one class and another (see Fig. 8), we also defined a hybrid class that consists of a linear superposition of starburst and spiral SED templates, with the contribution of the spiral SED varying from 10% to 90% in 10% steps. This hybrid class

describes the current mix of old and young stellar populations in a galaxy. We have not defined other hybrid classes such as the Seyfert 2+ starburst class, as Schmitt et al. have found that these two populations have rather similar radio-to-infrared properties. Twenty-seven objects were successfully classified with this technique (the averaged weighted χ is ≤ 1) except for seven (Table 3). Among the latter, four are unambiguously powerful AGNs, as evidenced from their optical spectra (see Fig. 5; Hammer et al. 1995), including a QSO (14.1303) and Seyfert 1 galaxies (14.0573, 14.1302, and 14.1567), and one is a H II region (14.1103). The 1 σ dispersion around the χ^2 value for each fit gives an idea of the reliability of our classification scheme (Fig. 9 below).

4.3. Final Classification of the $z \leq 1$ 15 μm Radio Sources

Among the 27 objects selected either at radio or 15 μm, we find seven ambiguous cases, generally in the classes between Seyfert 2 and S+SBH (Table 3). Table 4 summarizes all the information derived from their optical spectra and radio observations (spectral index and imagery). For three objects, emission lines or radio properties remove the ambiguity of the classification: 14.0779 shows a low ionization spectrum, and both 14.1028 and 14.1041 have negative radio spectral indexes and radio emission extending much beyond their optical sizes. The validity of our classification scheme is illustrated in Figure 8, which emphasizes the relevance of the ($B - 7$ μm, 2800 Å $- B$) color-color diagram as a diagnostic diagram for distinguishing starbursts from AGNs. In that diagram, starbursts lie in a well defined color-color region, while AGN-powered sources are around the starburst region. The object with the smallest ($B - 7$ μm) color is 14.9025, which is classified as a LINER.

Five galaxies, all within the 15 μm sample, are classified as pure SBHs. They are generally radio sources and were classified by Hammer et al. (1995) as being star-forming S+A objects. Figure 10 displays their SEDs, on which is superposed the SBH SED from Schmitt et al. The interpolated luminosity at the 60 μm bump and the 60 μm luminosity derived from the radio-FIR correlation ($S_{60\mu m} = 125 S_{5Ghz}$; Franceschini et al. 1994) agree to within 20% on average. Nine objects, seven of which are in the 15 μm sample, are classified as the superposition of a starburst with a spiral SED (Fig. 11). For all of them but one (14.0846) the starburst component dominates, providing more than 70% of the object bolometric luminosity (see Table 3). Only half of these objects are detected at radio wavelengths (Fig. 7), so they have likely lower star formation rates than pure SBHs. It has been widely argued that powerful starbursts such as those discovered by *IRAS* could contain an AGN that can contribute to their infrared luminosities (Sanders et al. 1988). In addition to the fact that their energy distributions and colors are typical of those of starbursts, it is unlikely that the starbursts described here are significantly contaminated by an AGN, because: Their IR luminosities ($L_{IR} < 2 \times 10^{12} L_\odot$; see Table 4) are lower than those of the ultraluminous IRAS galaxies. Local galaxies with those luminosities are mainly star-forming galaxies (Lutz et al. 1998); their radio spectral indices range from 0.4 to 1 between the observed frequencies of 1.4 and 5 GHz. This implies a thermal-to-nonthermal energy ratio in the rest frame of 0–0.2, in good agreement with the starburst population studied by Condon (1992); their radio
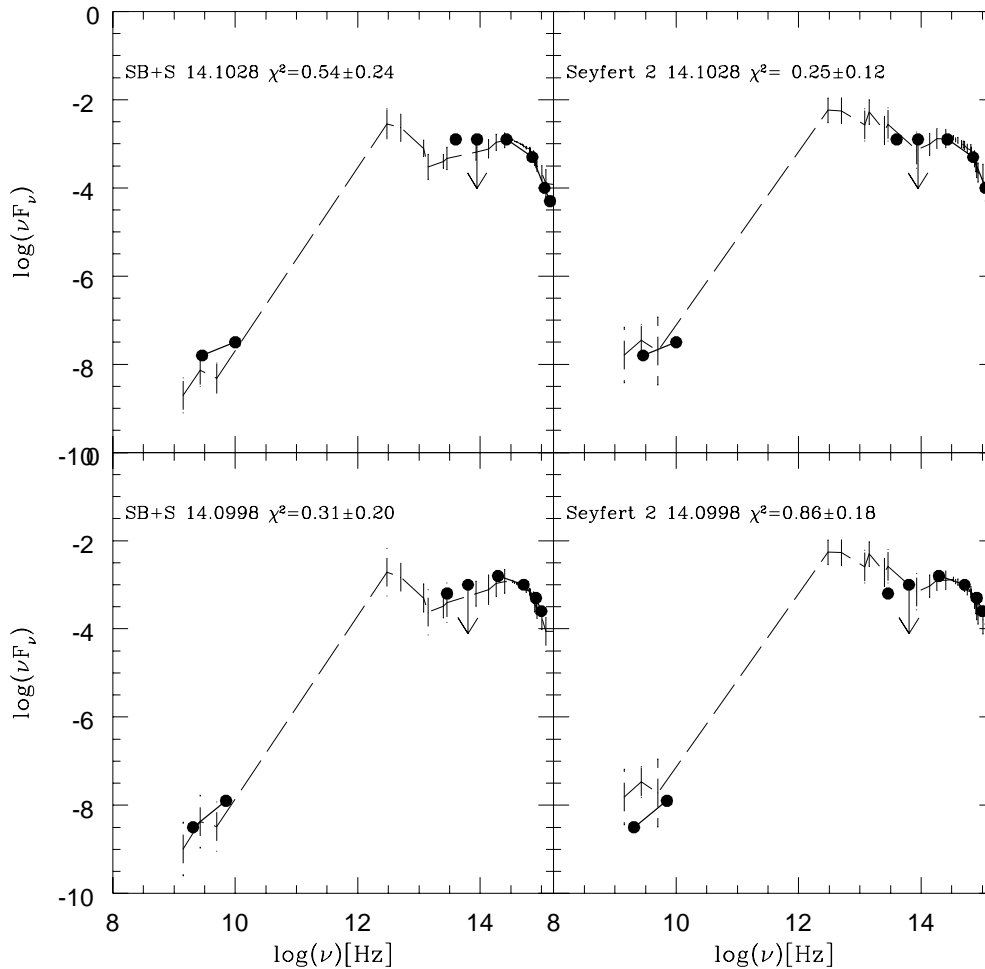
FIG. 9.—Some examples of possible ambiguous classifications of the SED. Solid dots represent flux measurements and are superposed to a template from Schmitt et al. Corresponding χ^2 values are indicated (see text).

angular sizes (less than 2″) are always in agreement with their optical sizes, as expected if star formation was distributed over the galaxy; and five of them have $z \leq 0.7$ and their spectra from CFRS have [O III] 5007 and Hβ emission lines; they all show low ionization spectra, with a prominent [O II]3727 line and, for all but one, no [O III] 5007 line. Figure 12 shows the sum of the five spectra, which reveals a red spectrum with [O II] 3727/H$\beta \sim 1$ and [O III] 5007]/H$\beta \leq 0.05$. These galaxies undoubtedly have emission-line spectra typical of H II regions, not AGNs.

Six objects, three of which are in the 15 μm sample, are classified as Seyfert 2 galaxies and four, two of which are in the 15 μm sample, are powerful AGNs (Seyfert 1 and QSO). Their SEDs are shown in Figure 13 as well as that of the radio LINER 14.9025, on which are superposed Schmitt et al. templates or radio-quiet QSO SEDs from Sanders et al. (1989). The two remaining objects are 14.1103, an H II galaxy, and 14.0820, an elliptical or a spiral galaxy with moderate star formation activity [W_0(O II) = 16 Å]. The object 14.1103 ($z = 0.21$) is detected at 15 μm but not at radio wavelengths, and its SED is consistent with that of a local H II region. This is in agreement with the absence of an old stellar component as noted by Tresse et al. (1993) from the very large Hα equivalent width (greater than 2500 Å). A *HST* image (Fig. 6) shows an unresolved object, giving a diameter less than 250 pc. We are probably witnessing here

a compact system undergoing one of its very first bursts of star formation: [O II]$_{3727}$ is not detected, while [O III]$_{5007}$ is very prominent. This galaxy shows spectral properties similar to those of a primordial galaxy, according to Tresse et al. (1993). Those authors derived a low heavy-element abundance (≤ 0.05 solar) and a large effective temperature ($T > 50,000$ K, based on the [O III]$_{4363}$/[O III]$_{5007}$ ratio).

5. GLOBAL UV AND IR LUMINOSITIES

5.1. *Global UV Luminosity*

L_{2800} values have been interpolated from L_{4350} and $(V - I)_{AB}$ [or $(B - I)_{AB}$] colors, using a grid of models with exponentially decreasing SFR ($\tau = 1$ Gyr; Bruzual & Charlot 1995) and a Salpeter initial mass function [IMF; $dN(m)/dm = -2.35$ over $m = 0.1$–100 $M_\odot$]. These calculations are found to be rather independent of the exact value of τ, except for very small values ($\tau \ll 0.1$ Gyr). We have calculated the total L_{2800} (see Table 5) in the CFRS 1415 + 52 field. It is based on 143 galaxies that have been spectroscopically identified and are representative of the 558 $I < 22.5$ galaxies in the field (see Lilly et al. 1995b). Converted to a luminosity density, this value is in excellent agreement (to within 6%) with that found for the whole CFRS field (Lilly et al. 1996). This is consistent with the

TABLE 4

PROPERTIES OF THE NONSTELLAR ISOCAM LW3 AND RADIO SOURCES WITH REDSHIFT

CFRS	z	$W_0(\text{O II})$ (Å)	D3538	$F^2_{7\,\mu m}$	$F_{15\,\mu m}$ [a]	$F_{5\,GHz}$ [b]	L_{2800} [c]	L_{IR} [c]	SFR_{IR} [d]	Spectral Class	SED Class [e]	α [f]	Angular Size [g]	Final class	Morphological Classification
								Sources detected at 15 μm and 5 GHz							
14.0227...	0.772	0.0	0.16	<150	274	<16	1.54	31.5 ± 7.2	54.6 ± 20.6	Quies	SB+S	...	...	SB+S	E[h]
14.0272...	0.668	14.3	0.20	<150	415	<16	1.54	35.9 ± 8.6	60.3 ± 11.4	S+A	SB+S	...	...	SB+S	C[h]
14.0663...	0.743	4.8	0.27	<150	275	20	0.99	127.5 ± 4.8	213.1 ± 17.8	S+A	SBH	0.8 ± 0.3	1.1	SBH	C[h]
14.0779...	0.578	31.3	0.27	<150	357	<16	0.22	39.7 ± 0.8	63.3 ± 2.5	S+A	Seyfert 2 /SBH	...	...	SBH	C[h]
14.0818...	0.899	22.1	0.20	<150	231	<38	2.13	50.2 ± 5.9	86.6 ± 10.1	S+A	SB+S	0.7 ± 0.2	...	SB+S	C[h]
14.0820...	0.976	16.4	0.19	<150	284	33	0.03	12.7 ± 1.0	...	S+A	S	1.0 ± 0.2	<1.3	S	...
14.0846...	0.989	43.0	0.24	<150	350	<16	1.15	28.9 ± 2.2	49.4 ± 10.3	S+A	SB+S/Seyfert 2	...	...	SB+S/Seyfert 2	Int
14.0909...	0.978	18.7	0.34	<150	347	<16	0.39	46.0 ± 40.	...	S+A	Seyfert 2	...	...	Seyfert 2	C[h]
14.0998...	0.430	11.8	0.43	<150	343	<26	0.20	5.7 ± 0.4	10.4 ± 5.2	S+A	SB+S	0.7 ± 0.3	...	SB+S	E[h]
14.1028...	0.988	18.6	0.22	<150	413	31	0.61	205.0 ± 25.7	...	S+A	Seyfert 2/SB+S	−0.2 ± 0.3	20	Seyfert 2	SO/a
14.1042...	0.875	17.0	0.23	176	231	<16	0.28	10.1 ± 0.8	17.3 ± 3.0	S+A	SB+S/Seyfert 2	...	...	SB+S/Seyfert 2	SO/a
14.1103...	0.209	0.0	...	<150	329	<16	0.03	1.3 ± 0.3	...	H II	H II	...	...	H II	C
14.1129...	0.831	...	...	207	292	<16	1.38	26.5 ± 2.6	45.4 ± 13.5	...	S+SB/Seyfert 2	...	...	S+SB	Int
14.1139...	0.660	19.3	0.23	161	787	79	1.38	157.5 ± 0.5	280.6 ± 1.8	S+A	SBH	0.5 ± 0.1	1.9	SBH	Int
14.1190...	0.754	16.0	0.30	<150	259	24	0.87	121.2 ± 7.9	215.9 ± 32.3	S+A	SBH	0.8 ± 0.2	1.6	SBH	Sab
14.1302...	0.548	19.7	0.14	<150	263	<16	0.86	6.5 ± 2.5	−	S	Seyfert 1	...	...	Seyfert 1	S[h]
14.1329...	0.375	13.5	0.18	153	485	70	0.26	62.8 ± 3.1	112.5 ± 10.8	S+A	SBH	0.8 ± 0.1	0.9	SBH	SO
14.1567...	0.479	0.0	−0.02	<150	642	<16	4.19	6.5 ± 2.5	−	Seyfert 1	Seyfert 1	...	...	Seyfert 1	...
14.9154...	0.812	38.7	0.34	230	425	39	0.64	130.1 ± 11.3	−	S+A	Seyfert 2	0.3 ± 0.2	1.5	Seyfert 2	...
								Radio sources not detected at 15 μm							
14.0276...	0.746	...	0.32	<150	<250	37	0.57	16.2 ± 1.6	−	E	SB+S	<−0.4	10	Seyfert 2	...
14.0573...	0.010	...	...	174	<250	37	0.57	11.1 ± 0.5	...	Seyfert 1	Seyfert 1	−0.8 ± 0.7	5 × 3	Seyfert 1	E
14.0727...	0.463	32.2	0.28	<150	<250	14	0.54	11.3 ± 2.8	19.4 ± 3.3	S+A	SB+S	1.0 ± 0.3	1.3	SB+S	...
14.0854...	0.992	0.0	0.13	<150	<250	35	0.08	26.3 ± 3.9	44.9 ± 7.1	Quies	SB+S/Seyfert 2	0.0 ± 0.3	<1.3	SB+S/Seyfert 2	SO/a
14.0937...	0.838	7.6	0.04	<150	<250	1311	0.39	131.3 ± 16.3	−	S+A	Seyfert 2	−0.1 ± 0.1	<0.2	Seyfert 2	E
14.1041...	0.372	56.0	0.30	<150	<250	47	0.28	8.0 ± 3.2	−	S+A	Seyfert 2/SB+S	−0.4 ± 0.4	15 × 10	Seyfert 2	Irr
14.1303...	0.985	...	...	<150	<250	45	22.20	115.7 ± 34.7		QSO	QSO	0.5 ± 0.2	<1.6	QSO	...
14.9025...	0.155	...	...	243	<250	47	0.12	5.8 ± 2.8		Liner	Liner	−0.4 ± 0.4	15 × 10	Liner	Scd

[a] Fluxes corrected by aperture effects in μJy.
[b] Flux at 5 GHz in μJy from Fomalont et al. 1992.
[c] 2800 and IR (8–1000 μm) luminosities in $10^{10}\, L_{\odot}$.
[d] IR star formation rate in $M_{\odot}\, yr^{-1}$.
[e] SED classification. See Table 3.
[f] Radio spectral index, between 1.5 and 5 GHz, from Fomalont et al. 1992.
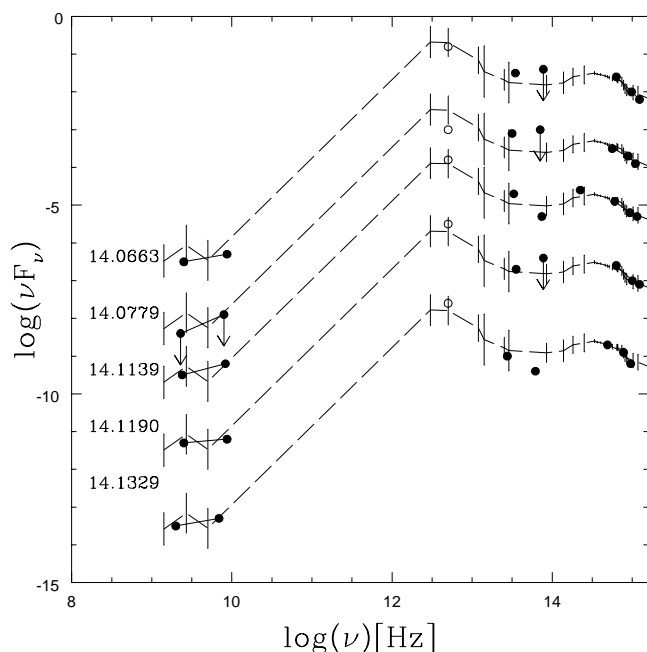[g] Angular size in arcseconds from Fomalont et al. 1992.
[h] From Schade et al. 1996.

These should be compared with their 2800 Å luminosities that range from 4×10^8 to 2×10^{10} $L_\odot$ and are not very different from those of galaxies not detected at 15 μm and radio wavelengths. Thus, taking into account only the UV luminosity of the 15 μm and radio galaxies that are luminous, infrared sources would lead to severe underestimates of their actual star formation rates. Nearly half of the global infrared luminosity of 15 μm and radio galaxies is coming from seven sources (four SBHs and three Seyfert 2). These are detected at both wavelengths, except for the Seyfert 2 galaxy 14.0937. Estimates of infrared luminosities of these bright galaxies should thus not be affected strongly by source count biases or modeling uncertainties.

Accounting for the global luminosity is slightly complicated by the current observational status of the data. Hammer et al. (1995) and recent follow-up work have nearly completed the redshift identifications of the radio μJy sources. Among the 45 $I_{AB} \leq 22.5$ 15 μm sources that are not detected at radio wavelengths, only 16 possess a redshift from the CFRS. The latter have not been selected a priori for their infrared properties and can be considered as representative of the whole sample. In the calculation of the global luminosity, we have assumed three different scaling factors: 1 for luminous galaxies detected in radio and at 15 μm, 29/21 for galaxies detected only at radio wavelength and 45/16, for the galaxies, with an additional statistical error of 25%. Table 5 presents the different values of the global luminosities at 2800 Å and in the infrared after excluding powerful AGNs (QSO and Seyfert 1). At IR wavelengths, Seyfert 2 contribute to more than a third of the global luminosity.

5.2.3. Global IR Luminosity from Galaxies Undetected at 15 μm and Radio

We consider here the subsample of the 49 galaxies that possess a redshift, are not detected at 15 μm or radio wavelengths, and have been observed at K. This subsample can be taken as representative of the 489 $I_{AB} \leq 22.5$ galaxies not detected at 15 μm or radio wavelengths in the CFRS 1515 + 52 field. For these galaxies, we use $BVIK$ photometry and their 15 μm and radio upper limits to investigate their SEDs. We found that 19 of them have SEDs consistent with those of local template SEDs for SBH galaxies and 16 have local template SEDs for SBL galaxies. The relatively large fraction of SBLs is compatible with the fact that they are not detected in the MIR range. Other objects have their SEDs consistent with those of local template SEDs for E/S galaxies (nine objects) or AGN galaxies (five objects). The fraction of AGNs is in reasonable agreement with Hammer et al. (1997), who find that ~8% of all galaxies in the field at $z \sim 0.5$ are Seyfert 2 galaxies, as indicated by their emission-line ratios. Figure 14 displays four examples of fits for these

FIG. 10.—Comparison of the SEDs of five SBH galaxies (*filled circles*, separated by arbitrary vertical shifts) with a local averaged SBH SED (*dashed line*; from Schmitt et al. 1998). Fluxes at 60 μm (*open circles*) are derived from radio fluxes according to the radio-FIR correlation ($S_{60\mu m} = 125 S_{5\,GHz}$; Franceschini et al. 1994). Superposed to the fit are vertical bars that display at each wavelength the standard deviation of the local template. The bottom panel presents the standard deviation of the five SBHs.

Poisson error of 8% for the 143 representative galaxies.

5.2. Global IR Luminosity

5.2.1. Interpolated IR Luminosities

Infrared (8–1000 μm) luminosities are interpolated from our MIR and radio flux measurements by using the template from Schmitt et al. (1997) with the smallest χ^2 for each object. The template gives 5–7 points within the wavelength range of interest, and errors can be estimated for each object using our Monte Carlo simulations. Our quoted errors take into account flux measurements errors (13% on average) as well as uncertainties in our classification scheme (5% on average). The interpolated infrared luminosity for each object, along with its associated error, is given in Table 4.

5.2.2. Global IR Luminosity from Galaxies of the 15 μm and Radio Samples

Galaxies detected at 15 μm and/or radio wavelengths have infrared luminosities in the range of (5×10^{10})–(2×10^{12}) $L_\odot$ (Table 4), comparable with those of typical local starbursts and Seyfert 2 galaxies (Genzel et al. 1998).

TABLE 5

GLOBAL LUMINOSITIES $[10^{10} * L_\odot]$ OF THE CFRS 1415 + 52 FIELD

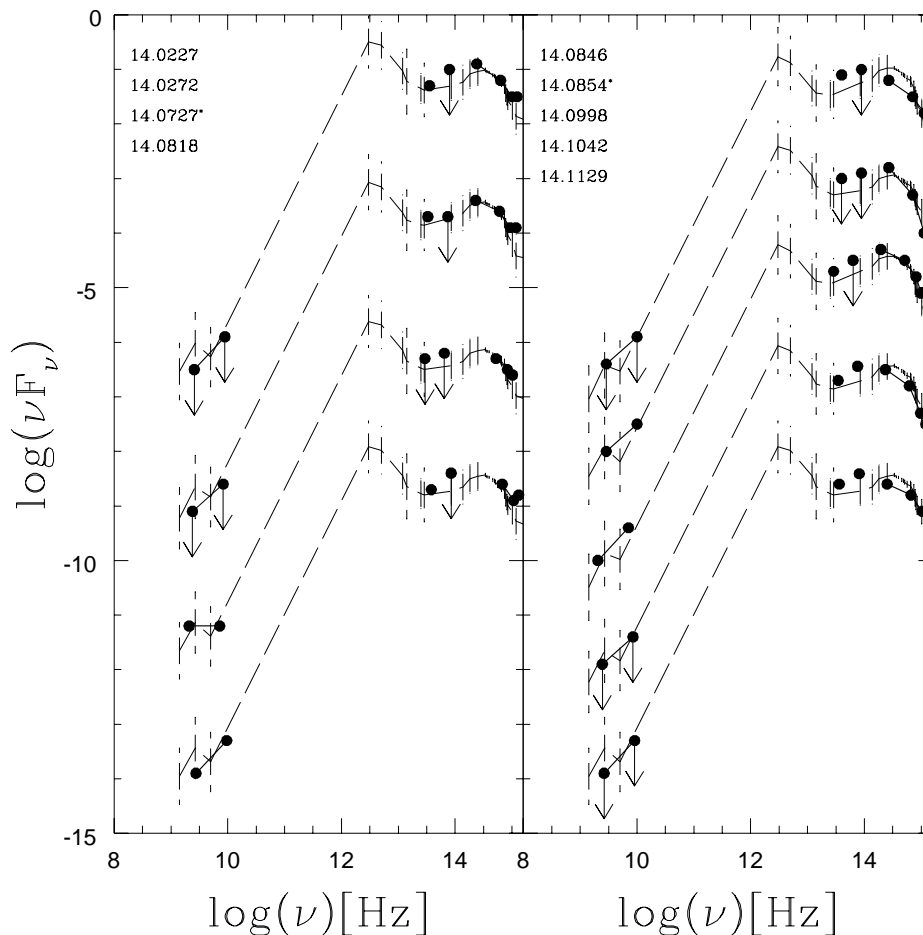|	15 μm-RADIO		NO DETECTED 15 μm-RADIO		CFRS 1415 + 52	
	L_{2800}	L_{IR}	L_{2800}	L_{IR}	L_{2800}	L_{IR}
Upper limit	29 ± 6	1778 ± 607	217 ± 29	2161 ± 214	246 ± 35	3939 ± 821
AGN contribution	4 ± 1	680 ± 291	17 ± 2	84 ± 27	21 ± 3	724 ± 318
"Old star" contribution......	1 ± 0	115 ± 28	25 ± 3	44 ± 16	26 ± 3	159 ± 44
Lower limit	24 ± 5	984 ± 288	175 ± 24	511 ± 71	199 ± 29	1495 ± 359

FIG. 11.—SED of galaxies classified as S + SB, separated by arbitrary vertical shifts, compared with SEDs of local spiral galaxies with a starburst component (S + SB; *dashed line*). The arrow indicates the radio flux limit (16 μJy) for some galaxies. Galaxies detected only at radio wavelengths are marked with an asterisk.
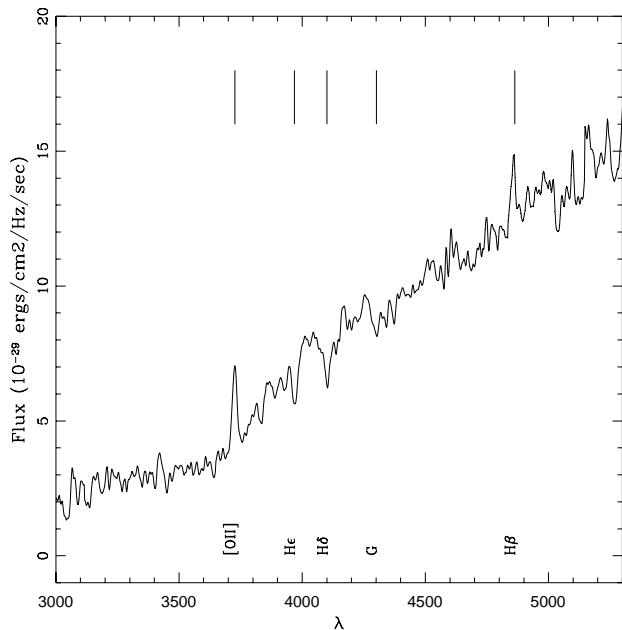
objects. All objects but four have been reasonably classified by this method. The four remaining objects have finally been classified as starbursts.

5.2.4. IR Luminosity Density Related to Star Formation and Uncertainties

The luminosity density of star-forming galaxies may be simply estimated by summing up the contribution of all starburst galaxies (SBH, SBL, and S + SBH) identified in the field. Uncertainties, which include errors in source counts, flux errors, and uncertainties in the identification, would come from our Monte Carlo simulations.

However, several complications could affect the validity of such a calculation. First, the origin of the UV and infrared light from Seyfert 2 galaxies is unclear and can be attributed either to the AGN, star formation, or both. Indeed, Seyfert 2 galaxies show a wide range in their infrared properties, and few color diagrams are able to distinguish them from starbursts. Contamination of the luminosity density by AGNs is potentially the most serious problem for any estimate of the star formation density. Second, cirrus can contribute to the infrared luminosity, and this is likely the case for the objects classified as S + SBH. It is often assumed that the 60 μm luminosity of apparently quiescent early-type galaxies is related to cirrus excited by the emission of the underlying stellar population (Sauvage
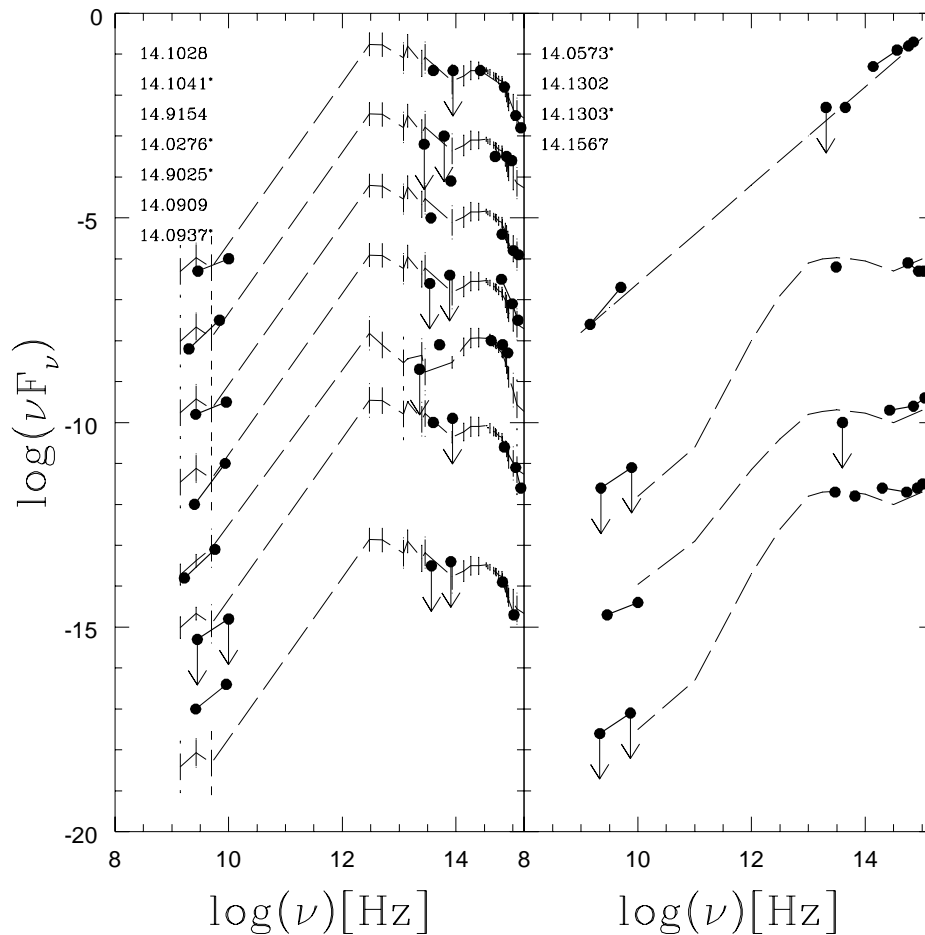
FIG. 12.—Average spectrum of the five SBH and S + SBH galaxies with $z < 0.7$. Spectral features are indicated. The average spectrum has been computed by using median values to account for luminosity variation from one object to another.

FIG. 13.—SED of AGNs detected with *ISO* at 15 μm compared with local SEDs. (*left*) All objects are compared with a Seyfert 2 SED template, except for 14.9025 (Liner SED template). (*right*) Powerful AGN (QSO and Seyfert 1) SEDs compared with power-law or radio-quiet QSO (Sanders et al. 1989). Galaxies detected only at radio wavelengths are marked with an asterisk and their fluxes at 15 μm by an arrow, assuming a upper limiting flux of 250 μJy.

& Thuan 1992). This is however disputed by Devereux & Hameed (1997), who present some counterexamples and argue that young stars can be an important source of the FIR light of early-type galaxies. One may wonder, however, about the exact nature of early-type galaxies with a significant population of young stars embedded in dust. Might they not be equivalent to our S + SBH galaxies? In that case, the cirrus contribution to the infrared luminosity of these galaxies cannot be significant, as the starburst component contributes to most of their bolometric luminosities.

Recall that former estimates of the SFR co-moving density from the UV light are uncertain because:

1. They include contributions at 2800 Å from AGNs and old stellar populations.

2. They do not account for the UV light reprocessed by dust into FIR radiation.

We wish here to take into account the deficiencies mentioned above and calculate *upper and lower limits to the luminosity density related to star formation*. The upper limit is obtained with the following assumptions:

1. The 15 μm and radio fluxes of all objects not detected at those wavelengths are set equal to their detection limit. This provides an upper limit to their infrared flux.

2. The 2800 Å and 60 μm luminosities of AGN-classified objects are assumed to be powered by star formation.

3. The infrared luminosities of S + SBH galaxies are assumed to be only coming from star formation.

The lower limit is obtained with the following assumptions:

1. All objects not detected at 15 μm and radio wavelengths have zero extinction, and hence the star formation rate estimated at infrared wavelengths equals that estimated at UV wavelengths.

2. The 2800 Å and 60 μm luminosities of AGNs and quiescent (E) galaxies are assumed to be related, respectively, to the active nucleus and the old stellar component.

3. The infrared luminosities of S + SBH galaxies are assumed to be related to both cirrus and star formation, in the proportion of the ratio of the bolometric luminosities of the two components.

Table 5 displays the global luminosities in the CFRS 1415 + 52 field as derived from UV (2800 Å) and infrared (8–1000 μm) fluxes for the sample of objects detected either at 15 μm or radio wavelengths and that containing objects not detected at both wavelengths. The AGN contributions are given in the upper limit case. They can attain non-negligible values ($\sim 20\%$), including at UV wavelengths. This represents a major uncertainty for the SF densities derived from UV fluxes. The errors take into account uncer-
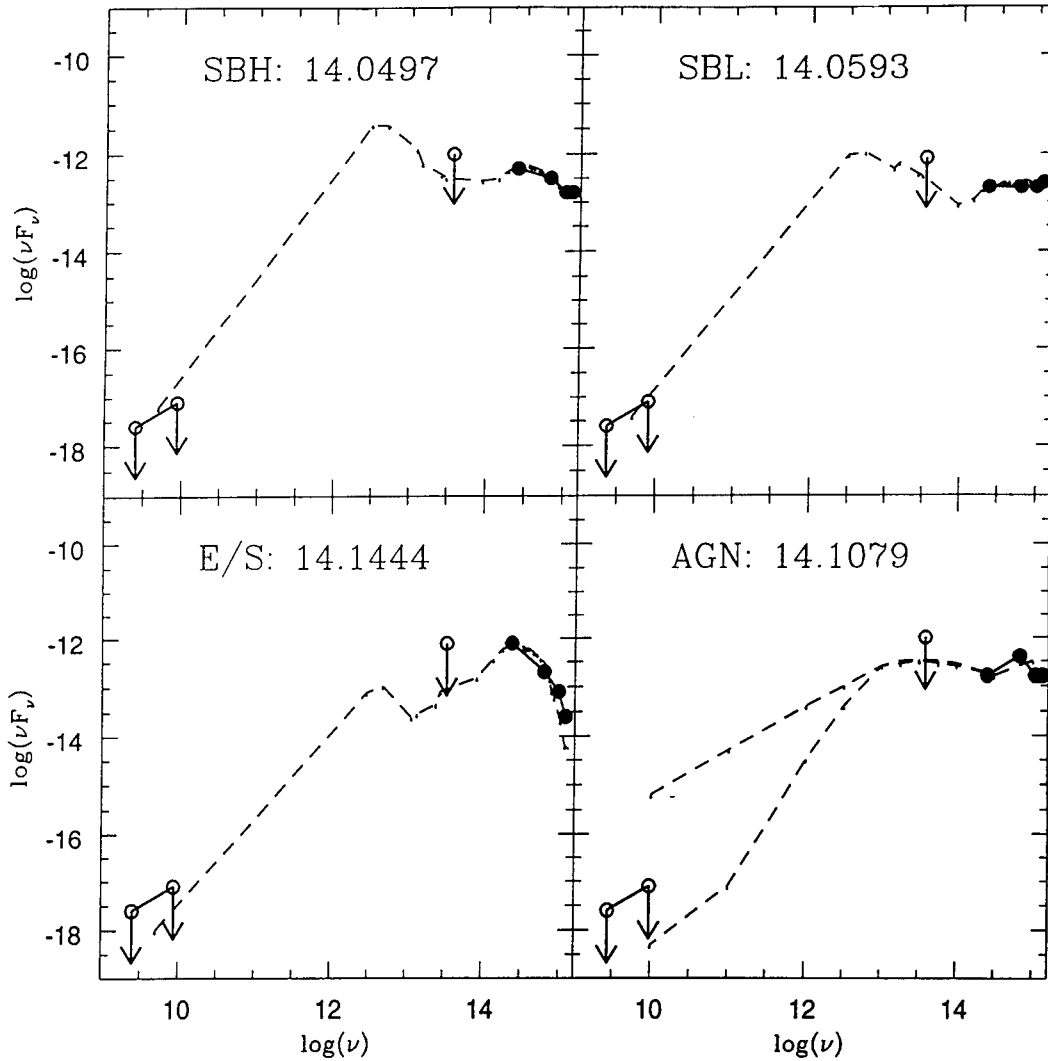
Fig. 14.—Four examples of the SED of galaxies that are not detected at 15 μm and radio wavelengths but possess $B - K$ observations.

tainties in source counts, flux measurements errors, and uncertainties in the classification scheme.

6. ESTIMATION OF THE COSMIC STAR FORMATION RATE

6.1. Star Formation Density Derived from the UV Light Density

The star formation history has been estimated by various authors (see Madau et al. 1996; Lilly et al. 1996; Hammer et al. 1997) on the basis of the CFRS and/or HDF surveys using star formation rates derived from 2800 Å or $[O\,\textsc{ii}]_{3727}$ fluxes. Since the UV light is dominated by emission from more or less massive stars, the total SFR as derived only from the flux at 2800 Å is somewhat uncertain, as the extrapolation to the low-mass end ($M \leq 5\ M_\odot$) of the IMF is not constrained. Moreover, Hammer et al. (1997) have suggested that dust and metallicity can severely affect these estimates and mask the true evolution of the cosmic star formation rate. We adopt in the calculation of the star formation rate (SFR) from the UV light the calibration of Madau et al. (1998) and Kennicutt (1998), assuming a Salpeter (1955) IMF with mass limits 0.1 and 100 $M_\odot$:

$$SFR_{2800} = 5.045 \times 10^{-10}(L_{2800}/L_\odot)\,. \tag{3}$$

6.2. Star Formation Density Derived from the IR Light Density

The SFR can also be inferred from infrared luminosities, assuming that they result mostly from dust heating by young stars in the optically thick limit. The SFR calibration depends mainly on the burst duration and IMF slope at both high- and intermediate-mass ranges. Following Kennicutt (1998), we adopt the same IMF as that assumed to calculate the SFR derived from UV light, and

$$SFR_{IR} = 1.71 \times 10^{-10}(L_{IR}/L_\odot)\,. \tag{4}$$

The above equation is based on the models of Lehnert & Heckman (1996) for a continuous burst with age 10–100 Myr. Condon (1992) calibrated the SFR from the nonthermal radio luminosity (L_{NT}), assuming the Galactic relation between L_{NT} and the radio supernova rate. He then derived the SFR_{IR} calibration from the FIR-radio correlation, showing that $\sim \frac{2}{3}$ of the UV-to-optical emission is re-emitted between 40 and 120 μm (see also Helou et al. 1988). After rescaling his value by assuming a Salpeter IMF (0.1–100 $M_\odot$), Condon (1992) obtains

$$SFR_{IR} = 2.22 \times 10^{-10}(L_{IR}/L_\odot)\,. \tag{5}$$

The difference between the two authors is at the 28% level, in agreement with the Kennicutt uncertainty estimate

of $\pm 30\%$ on his calibration, after comparison with other models (Hunter et al. 1986; Lehnert & Heckman 1996; Meurer et al. 1997).

The key parameter in these estimations is the star formation rate of massive stars (typically $\geq 5\ M_\odot$), which are mainly responsible for the UV continuum, the nonthermal radio continuum, and FIR luminosities reradiated by dust. The SFR_{IR}/SFR_{UV} ratio calculated in the following is essentially independent of the IMF slope and in particular of any extrapolation toward low stellar masses.

6.3. *Star Formation Density Missed by UV Observations*

We aim to calculate here the cosmic SFR from the infrared emission and compare it with that derived from the UV emission. We first consider the "directly observed" SFR, based on observations of the $I_{AB} \leq 22.5$ galaxies, as presented by Lilly et al. (1996). In § 5.1 we have calculated the total L_{2800} contributed by all galaxies with $I_{AB} \leq 22.5$ and $z \leq 1$. In § 5.2 we have computed the total L_{IR} from those galaxies with either $S_{15\mu m} \geq 250$ or $S_{5GHz} \geq 16\ \mu Jy$ and from CFRS galaxies not detected at 15 μm and radio wavelengths.

We have calculated the SFR_{IR}/SFR_{2800} ratio, accounting for all galaxies not classified as powerful AGNs. It ranges from 2.5 ± 0.95 in the lower limit case to 5.4 ± 1.9, when galaxies undetected at 15 μm and in radio have their fluxes at these wavelengths equal to the detection limit. These values can, however, be affected by uncertainties on the calibration of the SFR in the UV and FIR wavelength ranges. Nevertheless, the values we find for SFR_{2800} and SFR_{IR} show some consistency, since for all galaxies SFR_{IR} is larger than SFR_{2800}. These ratios give extinctions ranging from $A_V = 0.49$ to 0.87 if we assume a standard galactic extinction law. If the true SFR density is given by the FIR estimation, then from 35% to 85% of the global SFR co-moving density for $z \leq 1$ is not taken into account when only the UV flux density is considered.

Figure 15 shows the co-moving SFR density evolution with look-back time (for $H_0 = 50$ km s^{-1} Mpc^{-3} and $q_0 = 0.5$). The VLA-*ISO*-CFRS points (*filled dots*) represent the average values of the upper and lower limits defined above. Since there is no evidence for a change in the extinction for $z \leq 0.5$ as compared with $0.5 < z \leq 1$, we have adopted the same redshift bins as those used in previously deriving the SFR from the UV fluxes. VLA-*ISO*-CFRS data are 2.9 ± 1.3 larger than former UV estimated values, even though the latter accounted for all sources, including strong AGNs. The error bars account for incompleteness errors (Lilly et al. 1996) as well as uncertainties in the determination of the SFR density at IR wavelengths.

Error bars in Figure 15 are very large mostly because we have assumed that the blue galaxies undetected at 15 μm and radio wavelengths have no extinction (lower limit case) or have flux densities equal to the detection limits (upper limit case), both of which are clearly unrealistic assumptions. It is interesting to check whether our average value makes sense. Starbursts detected by both ISOCAM and the VLA are rare. They have large extinctions ranging from $A_V = 1.5$ to 2 and show red continua (Fig. 12). Tresse & Maddox (1998) predict an extinction of 1 mag at 2800 Å (or $A_V = 0.48$) for the blue field galaxy population at $z \leq 0.3$. If the same value holds on average for blue galaxies up to $z = 1$, we can predict in principle the infrared luminosity of the field galaxy population not detected at 15 μm and radio wavelengths. For them, Table 5 gives an average value
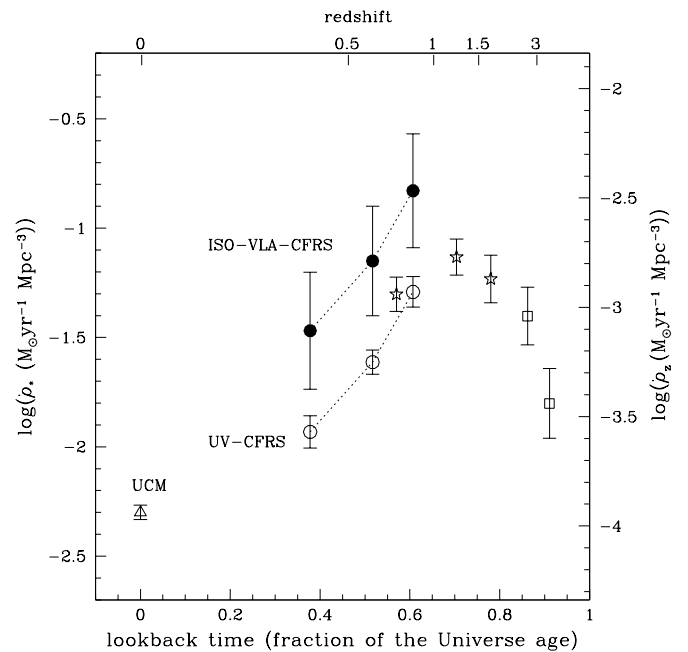

FIG. 15.—Metal production and star formation history for $z \leq 1$ (see text). Our points (*filled circles*, labeled *ISO*-VLA-CFRS) are 2.9 times higher in SFR density or in metal production than those (*open circles*) previously derived from the UV flux density at 2800 Å. Other points are from Gallego et al. (1995; *open triangle*), Connolly et al. (1997; *open stars*), Madau et al. (1998; HDF; *open squares*) and have not been corrected for extinction.

$L_{2800} = 196 \times 10^{10}\ L_\odot$ in the field. According to equation (3), this corresponds to a global SFR_{2800} of 980 $M_\odot$ yr^{-1}. Adopting the Tresse & Maddox extinction estimate, the global infrared luminosity would be equal to 1445×10^{10} $L_\odot$ (equation 4). This is in very good agreement with the average value in the fourth column of Table 5 and adds more confidence in the VLA-*ISO*-CFRS average values shown in Figure 15.

These average values imply that the stellar mass formed, since $z = 1$ would be $3.3 \times 10^8\ M_\odot$ Mpc^{-3}, slightly larger than the estimation of the present-day stellar mass of $3 \times 10^8\ M_\odot$ Mpc^{-3} (Cowie et al. 1996; Glazebrook et al. 1995). Of course, the uncertainties on the SFR estimations are large, and our lower estimate is still consistent with the present day stellar mass. However, we believe that this will constitute a serious problem, when uncertainties will be lowered by larger and deeper surveys at infrared and radio wavelengths. The problem gets worse if one accounts for the additional star formation at $z > 1$. There may be two ways out. First, half of the SFR density comes from $\sim 10\%$ of the field galaxies, those detected at 15 μm and radio wavelengths. These objects with large SFR (especially those with greater than 100 $M_\odot$ yr^{-1}) may have IMFs that significantly deviate from the Salpeter law. Alternatively, the local stellar mass density may have been systematically underestimated.

7. COMPARISON WITH THE HDF/ISOCAM SURVEYS

The number densities of faint MIR and radio sources found in the CFRS 1415 + 52 field and the HDF appear to be a reasonable agreement. However, our results are not consistent with those derived for the HDF by Rowan-Robinson et al. (1997). The HDF is 18.5 smaller in area than

the CFRS 1415 + 52 field, and from our results we would expect 0.3 starbursts with SFR larger than 100 $M_\odot$ yr^{-1}, as compared with the four starbursts with SFRs from 500 to 1010 $M_\odot$ yr^{-1} claimed by Rowan-Robinson et al. (1997). No simple explanation can account for this discrepancy of more than 1 order of magnitude. The calibration of the SFR$_{FIR}$ by Rowan-Robinson et al. (1997) differs slightly from ours (their proportionality factor in eq. [4] is 2.6×10^{-10} instead of our 1.7×10^{-10}). We simply stress that:

1. Our source detection and identification procedures are robust (see also Flores et al. 1998), while source identifications can be difficult in the HDF, since several galaxies in the HDF can lie within a single ISOCAM pixel.

2. Rowan-Robinson et al. (1997) have used a three-component model (a stellar component giving rise to the UV-to-MIR emission plus cirrus and starburst components, giving rise to the MIR-to-radio emission) to fit galaxy SEDs. This type of model has several degrees of freedom, including the relative energy ratio between the different components. The number of free parameters is larger than the number of available data points (1–3) in the MIR-to-radio wavelength range.

3. Among the twelve HDF galaxies whose SEDs were fitted by Rowan-Robinson et al. (1997), five have limits on their radio luminosities that are significantly lower than the starburst model predictions (see their Fig. 1).

Instead of force-fitting the data points by multiple-parameter starburst models, we propose here a more conservative empirical approach of fitting SEDs of galaxies with $z \leq 1$ with SED templates of well-studied local galaxies (see Schmitt et al. 1997). The fits are generally quite good, especially for starburst (SB) SEDs that are consistent with the standard radio-FIR correlation. A pure starburst has its energy distribution dominated mostly by star formation. Its SED includes massive star light with or without extinction at UV wavelengths, re-emission of the absorbed UV light at MIR and FIR wavelengths, and starburst thermal emission and synchrotron radiation from supernova remnants at radio wavelengths. Locally, Schmitt et al. (1997) show that starbursts, when compared with normal spirals or ellipticals, have a smaller spread in their SEDs from FIR to radio wavelengths. There is no evidence that these properties change significantly in the redshift range $0 \leq z \leq 1$.

Strong starbursts (with SFRs larger than 70 $M_\odot$ yr^{-1}) should be detected by deep radio surveys to μJy levels, such as those by Fomalont et al. (1991) in the CFRS 1415 + 52 field or Fomalont et al. (1997) in the HDF. The fact that these are not detected in the HDF at radio wavelengths casts some doubt on the large SFRs derived by Rowan-Robinson et al. (1997) for objects without radio counterparts. As for the three radio sources with $S_{5GHz} \geq 16$ μJy and $z \leq 1$ that are found in the HDF (Fomalont et al. 1997), one (ISOHDF 12 36 46 + 62 14 06, $z = 0.96$) is found by Rowan-Robinson et al. (1997) to have the highest SFR (1010 $M_\odot$ yr^{-1}) in their sample. It is at $z = 0.96$, has an elliptical morphology, is undetected at 15 μm (as most of the elliptical galaxies of the Hammer et al. 1995 radio sample) and shows highly ionized emission typical of a Seyfert galaxy (Mg II λ2799, [Ne v] λ3426, and [Ne III] λ3868). It is likely a Seyfert 1 galaxy, since the Mg II line is broad and its radio emission shows some variability (Richards et al. 1998). It is doubtful that its emission is powered by star formation.

To derive FIR luminosities (and hence SFRs) requires complete information from UV-to-radio wavelengths. It seems reasonable to use templates based on well-known local objects, especially for the most powerful star-forming galaxies.

8. CONCLUSIONS

Observations of distant field galaxies have been obtained with ISOCAM down to unprecedented flux levels at 6.75 ($S \geq 150$ μJy) and 15 μm ($S \geq 250$ μJy). We have attempted to make our samples at both those wavelengths as complete as possible by a careful reduction of the data. That the samples are complete is suggested by the good positional correlation between source identifications at 6.75 and 15 μm and radio wavelengths.

Source densities are comparable at 6.75 μm (1944 $S > 150$ μJy sources deg^{-2}; Flores et al. 1998), 15 μm (2808 $S > 250$ μJy sources deg^{-2}; this paper), and 5 GHz (1440 $S > 16$ μJy sources deg^{-2}; Fomalont et al. 1991). Star-forming objects contribute, respectively, 50%, 73%, and 26% of the extragalactic counts at 6.75 and 15 μm and 5 GHz. This suggests that the 60 μm luminosity density is strongly dominated by star-forming galaxies. The fraction of $z > 1$ objects is found to be less than 32%, 43%, and 40% of the extragalactic counts at 6.75 and 15 μm and 5 GHz, respectively. The 15 μm survey is found to be rather efficient in selecting high-redshift objects, since sources with $I_{AB} \leq 22.5$ and $S_{15\mu m} \geq 250$ μJy have a median redshift of 0.76, as compared with 0.59 for the whole CFRS.

The 15 μm survey, combined with radio and optical data, allows us to identify the most powerful star-forming objects (with SFRs larger than 100 $M_\odot$ yr^{-1}) in the field, at least up to $z = 1$. Four such objects (0.7%) are found among the 578 $I \leq 22.5$ galaxies, and they contribute to 18% of the SFR density. From their UV or [O II]$_{3727}$ emission-line properties, these objects cannot be distinguished from galaxies with more modest rates of star formation. If we correct for extinction, assuming that their optical spectra from 2500–4000 Å is reddened by the standard galactic extinction curve (with A_V derived from the SFR$_{IR}$/SFR$_{UV}$ ratio), they would appear as young starbursts with a moderate population of A stars [$W_0(H\delta) = 3.5$ Å in the combined spectrum]. The 15 μm sample contains highly reddened young starbursts as well as a larger number of galaxies (S + SB) with lower SFRs, which all contain a significant population of A stars (S + A galaxies). This is consistent with the scenario of strong starburst episodes followed by the last phases of the burst, where the IR emission is still high because of dust heating by intermediate-mass stars ($M = 1$–3 $M_\odot$; Lisenfeld, Volk, & Xu 1997).

The combination of 15 μm and radio samples probably gives a good representation of the galaxy population in a very deep 60 μm survey. Interpolated infrared (8–1000 μm) luminosities based on fits of galaxy SEDs by local templates from radio-to-UV wavelengths imply that 75% (-40%, $+10$%) of the star formation rate density for $z \leq 1$ is hidden by dust. No evidence has been found for an evolution of that fraction in the above redshift range. The global opacity of the universe up to $z = 1$ ranges from $A_V = 0.5$ to 0.85. A subsample of 16 15 μm galaxies observed by the *HST* indicates that more than a third of the star formation hidden by dust is associated with interacting galaxies or mergers.

Estimates of the SFR from UV fluxes carry some uncertainties because of two main reasons: one related to the UV

light reprocessed by dust into FIR radiation and the other to the probably important contribution of AGN light at UV wavelengths. In spite of the small statistics of the sample considered here, our work allows a first glimpse of the true SFR density for $z \leq 1$. From our careful data analysis and the use of multiwavelength data from radio-to-UV, we believe that the true SFR density lies within the region delimited by the still large error bars in Figure 15. Our average value, 70% of the star formation rate density hidden by dust, is consistent with a 1 mag absorption at 2800 Å for the blue galaxy population (see Tresse & Maddox 1998) and less than 4% of the galaxies being highly reddened, detected at 15 μm and radio wavelengths, and contributing to 50% of the global IR luminosity density.

Although our values are lower by a factor 2.8 than those of Rowan-Robinson et al. (1997), they might be too high

when the corresponding stellar mass formed, since $z = 1$ is compared with the present-day stellar mass density. This could raise an important question about the universality of the IMF, especially in the high-SFR galaxies detected by ISOCAM and the VLA and described in this paper. Studies of other CFRS fields with the same multiwavelength technique are needed to improve the source statistics, determine more accurately the SFR density, and study in more detail its redshift evolution.

REFERENCES

Brinchmann, J., et al. 1997, ApJ, 499, 112
Bruzual, G., & Charlot, S. 1995
Césarsky, C. J., et al. 1996, A&A, 315, L32
———. 1998, in preparation
Clements, D., et al. 1998, preprint (astro-ph/9809054)
Condon, J. 1992, ARA&A, 30, 575
Condon, J., & Roderick, J. 1988, AJ, 96, 30
Connolly, A., Szalay, A., Dickinson, M., SubbaRao, M., & Brunne, R. 1997, ApJ, 486, L11
Cowie, L., Hu, E., Songaila, A., & Cohen, J. 1996, ApJ, 112, 839
Désert, F. X., et al. 1998, A&A, in press
Devereux, N., & Hameed, S. 1997, AJ, 113, 599
Elbaz, D., et al. 1998, preprint (astro-ph/9807209)
Flores, H., et al. 1998, A&A, in press
Fomalont, E. B., et al. 1997, ApJ, 475, L5
Fomalont, E. B., Windhorst, R. A., Kristian, J. A., & Kellerman, K. I. 1991, AJ, 102, 1258
Franceschini, A., et al. 1991, A&AS, 89, 285
Franceschini, A., Mazzei, P., Zotti, G., & Danesse, L. 1994, ApJ, 427, 140
Gallego, J., Zamorano, J., Aragon-Salamanca, A., & Rego, M. 1995, ApJ, 455, 1
Genzel, R., et al. 1997, preprint (astro-ph/9711255)
Glazebrook, K., et al. 1998, preprint (astro-ph/9808276)
Glazebrook, K., Peacock, J., Miller, L., & Collins, C. 1995, MNRAS, 275, 169
Groth, E., et al. 1994, BAAS, 185, 5309
Hammer, F., Crampton, D., Lilly, S., Le Fèvre, O., & Kenet, T. 1995, MNRAS, 276, 1085
Hammer, F., et al. 1997, ApJ, 480, 59
Hammer, F., Schade, D., Crampton, D., Lilly, S., & Le Fèvre, O. 1996, in Science with the *Hubble Space Telescope* II, ed. P. Benvenuti et al. (Baltimore: STScI), 101
Helou, G., Khan, I., Malek, L., & Boehmer, L. 1988, ApJS, 68, 151
Hunter, J., Sandford, M., Whitaker, R., & Klein, R. 1986, ApJ, 305, 309

Kennicutt, R. 1992, ApJ, 388, 310
Kennicutt, R., Jr. 1998, ApJ, 498, 541
Kessler, M. F., et al. 1996, A&A, 315, L27
Laurant, O., & Mirabel, F. 1998, in preparation
Lehnert, M., & Heckman, T. 1996, ApJ, 472, 546
Leitherer, M., Fergunson, H., & Heckman, T. 1995, A&AS, 186, 3004
Lilly, S., Le Fèvre, O., Crampton, D., Hammer, F., & Tresse, L. 1995a, ApJ, 455, 50
Lilly, S., Le Fèvre, O., Hammer, F., & Crampton, D. 1996, ApJ, 460, L1
Lilly, S. J., Hammer, F., Le Fèvre, O., & Crampton, D. 1995b, ApJ, 455, 75
Lisenfeld, U., Volk, H., & Xu, C. 1996, preprint (astro-ph/9605118)
Lutz, D., et al. 1998, ApJ, 505, 103
Madau, P., et al. 1996, MNRAS, 283, 1388
Madau, P., Pozzetti, L., & Dickinson, M. 1998, ApJ, 498, 106
Meurer, G., et al. 1997, AJ, 114, 54
Moshir, M. 1989, IRAS Faint Source Survey, Explanatory Supp. v. 1 (Pasadena: CalTech)
Puget, J., et al. 1998, in preparation
Richards, E., et al. 1998, AJ, 116, 1039
Rowan-Robinson, M., et al. 1997, MNRAS, 289, 490
Salpeter, E. 1955, ApJ, 121, 161
Sanders, D., et al. 1988, ApJ, 328, 35
———. 1989, ApJ, 347, 29
Sauvage, M., & Thuan, T. X. 1992, ApJ, 396, L69
Schade, D., Crampton, D., Hammer, F., Le Fèvre, O., & Lilly, S. J. 1996, MNRAS, 278, 95
Schmitt, H., Kinney, A., Calzetti, D., & Storchi-Bergmann, T. 1997, AJ, 114, 592
Spinoglio, L., et al. 1995, ApJ, 453, 616
Spinoglio, L., & Malkan, M. 1989, ESA/IRSA 343
Tresse, L., Hammer, F., Le Fevre, O., & Proust, D. 1993, A&A, 277, 53
Tresse, L., & Maddox, S. J. 1998, ApJ, 495, 691
Wrobel, J., & Heeschen, D. 1988, ApJ, 335, 677